

THE EFFECT OF CLAY TYPE ON THE PROPERTIES OF COHESIVE SEDIMENT GRAVITY FLOWS AND THEIR DEPOSITS

MEGAN L. BAKER,¹ JACO H. BAAS,¹ JONATHAN MALARKEY,¹ RICARDO SILVA JACINTO,² MELISSA J. CRAIG,³ IAN A. KANE,⁴ AND SIMON BARKER⁵

¹*School of Ocean Sciences, Bangor University, Menai Bridge, Anglesey LL59 5AB, U.K.*

²*IFREMER, Laboratoire Géodynamique et Enregistrement Sédimentaire, BP70, 29280 Plouzané, France*

³*Australian School of Petroleum, University of Adelaide, Adelaide SA 5005, Australia*

⁴*School of Earth and Environmental Sciences, The University of Manchester, Oxford Road, Manchester M13 9PL, U.K.*

⁵*Statoil ASA, Research Centre Bergen, NO-5020 Bergen, Norway*

e-mail: m.baker@bangor.ac.uk

ABSTRACT: The present knowledge of cohesive clay-laden sediment gravity flows (SGFs) and their deposits is limited, despite clay being one of the most abundant sediment types on earth and subaqueous SGFs transporting large volumes of sediment into the ocean. Lock-exchange experiments were conducted to contrast SGFs laden with noncohesive silica flour, weakly cohesive kaolinite, and strongly cohesive bentonite in terms of flow behavior, head velocity, runout distance, and deposit geometry across a wide range of suspended-sediment concentrations.

The three sediment types shared similar trends in the types of flows they developed, the maximum head velocity of these flows, and the deposit shape. As suspended-sediment concentration was increased, the flow type changed from low-density turbidity current (LDTTC) via high-density turbidity current (HDTTC) and mud flow to slide. As a function of increasing flow density, the maximum head velocity of LDTTCs and relatively dilute HDTTCs increased, whereas the maximum head velocity of the mud flows, slides, and relatively dense HDTTCs decreased. The increase in maximum head velocity was driven by turbulent support of the suspended sediment and the density difference between the flow and the ambient fluid. The decrease in maximum head velocity comprised attenuation of turbulence by frictional interaction between grains in the silica-flour flows and by pervasive cohesive forces in the kaolinite and bentonite flows. The silica-flour flows changed from turbulence-driven to friction-driven at a volumetric concentration of 47% and a maximum head velocity of 0.75 m s^{-1} ; the thresholds between turbulence-driven to cohesion-driven flow for kaolinite and bentonite were 22% and 0.50 m s^{-1} , and 16% and 0.37 m s^{-1} , respectively. The HDTTCs produced deposits that were wedge-shaped with a block-shaped downflow extension, the mud flows produced wedge-shaped deposits with partly or fully detached outrunner blocks, and the slides produced wedge-shaped deposits without extension. For the mud flows, slides, and most HDTTCs, an increasingly higher concentration was needed to produce similar maximum head velocities and runout distances for flows carrying bentonite, kaolinite, and silica flour, respectively. The strongly cohesive bentonite flows were able to create a stronger network of particle bonds than the weakly cohesive kaolinite flows of similar concentration. The silica-flour flows remained mobile up to an extremely high concentration of 52%, and frictional forces were able to counteract the excess density of the flows and attenuate the turbulence in these flows only at concentrations above 47%.

Dimensional analysis of the experimental data shows that the yield stress of the pre-failure suspension can be used to predict the runout distance and the dimensionless head velocity of the SGFs, independent of clay type. Extrapolation to the natural environment suggests that high-density SGFs laden with weakly cohesive clay reach a greater distance from their origin than flows that carry strongly cohesive clay at a similar suspended-sediment concentration, whilst equivalent fine-grained, noncohesive SGFs travel the farthest. The contrasting behavior of fine-grained SGFs laden with different clay minerals may extend to differences in the architecture of large-scale sediment bodies in deep marine systems.

INTRODUCTION

Sediment gravity flows (SGFs) are produced when gravity acts on the density difference between two fluids, and the excess density is provided by suspended sediment (Middleton and Hampton 1973; Kneller and

Buckee 2000). Subaqueous SGFs are volumetrically one of the most important sediment transport processes on our planet, providing large quantities of sediment to lakes, seas, and oceans (e.g., Kneller and Buckee 2000; Talling et al. 2015). As a result of their unpredictability and often large magnitude, SGFs can pose a significant threat to engineering works

TABLE 1.—Typical values of thickness, planar diameter, specific surface area, and cation exchange capacity of common clay minerals. Bentonite is part of the montmorillonite group of clay minerals. The clay minerals are sorted from small to large. Modified after Hillel (2004) and Yong et al. (2012).

Edge View	Typical Thickness (nm)	Planar Diameter (nm)	Specific Surface Area (SSA) (m ² /kg)	Cation Exchange Capacity (CEC) (mEq/100g)
Montmorillonite (incl. Bentonite)	2	10–1,000	700–800	80–100
Illite	20	100–2,000	80–120	10–40
Chlorite	30	100–2,000	70–90	10–40
Kaolinite	100	10–1,000	10–15	3–15

in deep water, such as drilling rigs and communication cables (Baas 2005). The deposits of these flows produce submarine fans, which are amongst the largest sedimentary bodies on Earth, and store the world's greatest reserves of oil and gas (Middleton 1993; Kneller and Buckee 2000; Baas 2005; Keevil et al. 2006). Much of what is known about SGFs originates from investigations in laboratory flumes (e.g., Sumner et al. 2009; de Leeuw et al. 2016), where controlled experiments provide a powerful method for understanding the flow dynamics. These laboratory studies complement descriptive core and outcrop studies, and state-of-the-art direct monitoring (Xu 2011; Sumner and Paull 2014; Xu et al. 2014). The majority of laboratory experiments have focused on sand-rich, noncohesive SGFs (e.g., Kuenen 1951; Parker et al. 1987; Middleton and Neal 1989; Baas et al. 2005), despite the fact that cohesive mud, made up of silt- and clay-size particles, is the most abundant sediment type on the Earth's surface (Hillier 1995; Healy et al. 2002; Schindler et al. 2015). It is therefore likely that mud is common in SGFs in the natural environment. Many examples of muddy, cohesive SGFs exist in the modern environment, such as at the mouth of the Zaire river in west-central Africa (Heezen et al. 1964; van Weering and van Iperen 1984; Droz et al. 2003), and in the ancient environment, such as in the Cretaceous Britannia Sandstone Member, North Sea (Barker et al. 2008), and in the Silurian Aberystwyth Grits of Cardigan Bay, Wales (Wilson et al. 1992; Talling et al. 2004).

Cohesive SGFs are more complex than noncohesive SGFs, because of the unique ability of suspended clay minerals to form flocs and gels (Winterwerp and van Kesteren 2004). Flocs are aggregates composed of clay particles that bind together when the attractive Van der Waals forces outcompete repulsive forces between the negatively charged surface of clay particles, often aided by the presence of positively charged ions in the water (Winterwerp and van Kesteren 2004). The presence of flocs in the flow increases the viscosity and yield stress and may thus affect the turbulence maintaining the flow (Baas and Best 2002). The amount of flocculation and the size of the flocs generally increase as the bulk suspended-clay concentration increases (Dyer and Manning 1999). Eventually, a "gelling" point may be reached at high clay concentration, which is characterized by the formation of a volume-filling network of particle bonds in the liquid (Blackbourn and Thomson 2000; Lowe and Guy 2000; Baas et al. 2009). A stable gel of linked clay minerals may be viscous enough to cause the total suppression of turbulence in the flow. Conversely, the electrostatic bonds between the clay particles can be broken in regions of high shear. Thus, an increase in turbulence generation in the flows by, for example, an increasing slope gradient has the potential to break up bonds between the clay particles and reduce the flow viscosity. This constantly shifting balance between turbulent and cohesive forces regulates the dynamic structure of cohesive SGFs (Baas et al. 2009).

The cohesive forces in a clay flow, i.e., its rheology, have been shown to change with clay concentration (Hampton 1975; Baas and Best 2002; Felix

and Peakall 2006; Baas et al. 2009; Sumner et al. 2009), but the type of clay mineral can also change the cohesive properties of the flow (Marr et al. 2001; Baas et al. 2016). Different clay minerals have different shapes, sizes, layer charges, cation exchange capacities, edge charge densities, and structures of the particle edges, which control the rheological and cohesive properties of the clay flow (Lagaly 1989). Some of these properties are also controlled by pH and the available ions in the medium (Luckham and Rossi 1999), which may vary independently of clay-mineral type.

The common clay minerals kaolinite and bentonite are end members in terms of cohesive properties, where kaolinite is weakly cohesive and bentonite is strongly cohesive, because of differences in chemical and physical properties (Table 1). Kaolinite particles are relatively large and have a low specific surface area (SSA), which is the ratio of the surface area of a material to either its volume or its mass (Table 1; Holtz and Kovacs 1981; Yong et al. 2012). The SSA of the particle controls the magnitude of the interparticle forces, with a larger SSA allowing greater interparticle forces (Atkinson 2007). Bentonite particles are relatively small and have a large SSA, which is further increased by the ability of bentonite to absorb water into its chemical structure. These water molecules separate unit layers in the clay mineral, causing it to expand, or swell, and thus increase the SSA (Yong et al. 2012). The cation exchange capacity (CEC) is a measure of the potential chemical activity of a clay mineral, which in turn is directly related to the cohesive forces (Kooistra et al. 1998; Khabbazi Basmenj et al. 2016). The high CEC of bentonite compared to kaolinite further explains its greater cohesive properties. Illite and chlorite are clay minerals with intermediate cohesive properties (Table 1), also commonly found in natural sediment. Illite and montmorillonite (which includes bentonite) are the most abundant clay minerals on the modern seafloor, each accounting for roughly 35% of the clay size fraction. Chlorite and kaolinite are less abundant, both accounting for approximately 15% of the clay size fraction (Griffin et al. 1968; Windom 1976; Hillier 1995).

Investigations of the effect of clay type on the dynamics of SGFs began recently. Marr et al. (2001) conducted an experimental study of sand-rich subaqueous gravity flows, which also carried bentonite or kaolinite clay, and found that 0.7% by weight of bentonite was sufficient to produce coherent flows, compared with 7% for kaolinite. Marr et al. (2001) defined coherent flows as flows that resist breaking apart and becoming completely turbulent under the dynamic stress associated with the head of a propagating debris flow. The lower threshold concentration of bentonite required to produce coherent gravity flows was attributed to the higher yield stress of bentonite mixtures compared to kaolinite mixtures of the same composition. Baas et al. (2016) found experimentally that the suspended-sediment concentration needed to produce transitional flow behavior (*sensu* Baas and Best 2002) is much lower in bentonite flows than in kaolinite flows. This was attributed to the greater cohesive strength of bentonite, producing flows with a significantly higher molecular viscosity and yield stress than kaolinite flows at concentrations above the gelling threshold.

The present paper provides further experimental evidence that clay type is an important control on cohesive SGFs. These experiments produced flows over a wide range of suspended-sediment concentrations to produce low-density turbidity currents, high-density turbidity currents, debris flows, and slides. The principal aims of this research were:

1. To determine how clay concentration and clay type qualitatively affect the flow properties and quantitatively affect the flow velocity, runout distance, and deposit geometry of fine-grained SGFs.
2. To investigate if the rheological properties of the pre-failure suspensions can be used to predict the flow velocity and runout distance of the laboratory SGFs, independent of clay type and concentration.

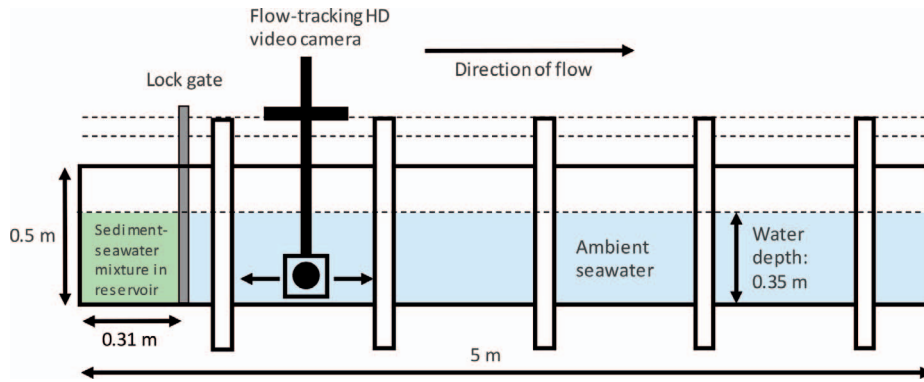


FIG. 1.—Experimental setup. HD, high-definition.

- To discuss the possible implications of the experimental data for natural SGFs and their deposits.

METHODS

Thirty-two laboratory experiments were conducted in a smooth-bottomed lock-exchange flume, 5 m long, 0.2 m wide, and 0.5 m deep (Fig. 1), using filtered seawater from the Menai Strait (NW Wales, U.K.) to better mimic flows in the deep ocean. Seawater contains a higher concentration of cations compared to freshwater, which helps reduce the repulsive forces between the negatively charged clay particles and enhance flocculation and gelling (Tan et al. 2014). In each experiment, the slope of the flume was set to 0° , and the reservoir was filled with a suspension of fine sediment and seawater, separated by a lock gate from the main compartment of the flume filled with seawater (density $\rho_a = 1.027 \text{ g cm}^{-3}$). The lock gate was then lifted to initiate the SGF. The experimental program comprised three different sediment types of contrasting rheological properties: (1) noncohesive silica flour ($D_{50} = 18.2 \text{ }\mu\text{m}$, density $\rho_s = 2650 \text{ kg m}^{-3}$) at initial volumetric sediment concentrations in seawater, C , of 1% to 52%; (2) weakly cohesive kaolinite ($D_{50} = 9.1 \text{ }\mu\text{m}$, $\rho_s = 2600 \text{ kg m}^{-3}$), ranging from $C = 1\%$ to $C = 29\%$, and; (3) strongly cohesive bentonite ($D_{50} = 5.6 \text{ }\mu\text{m}$, $\rho_s = 2300 \text{ kg m}^{-3}$), with C values between 1% and 20% (Table 2). These experiments examined the changes in the behavior of the SGFs as a function of suspended-sediment concentration and sediment type. Below, concentration always refers to volumetric concentration for the sake of succinctness.

In order to anticipate possible time-dependent behavior, a consistent method was used to prepare each suspension. First, half of the seawater and the sediment were mixed in a concrete mixer for 15 minutes. The remaining seawater and sediment were then added and the suspension was mixed for a further 15 minutes. Subsequently, the mixture was decanted into a container and further mixed by a handheld mixer for three minutes for kaolinite and silica flour and for 10 minutes for bentonite, to obtain a lump-free suspension. The suspension was then progressively added to the reservoir while the flume filled with seawater, in order to keep similar fluid levels on each side of the lock gate to limit pressure on the gate. Each flow was generated from the same volume and depth of mixture into a body of seawater of the same depth ($h = 0.35 \text{ m}$). The suspension in the reservoir was mixed using the handheld mixer for 60 s and then given $c. 10 \text{ s}$ to come to rest before lifting the gate and generating the SGF.

A time series of the head velocity of each SGF was obtained from the footage of a high-definition video camera that tracked the front of the flow along the length of the tank. The change in head position between the video frames was measured from the distance moved in pixels relative to a scale at the bottom of the flume, and velocity was then calculated using the timestamp of each frame. The flows were also recorded using a background

camera, set 4 m back from the tank to record a wide viewpoint, which captured changes in the evolution of the body and tail of the flow. The morphology of the SGF deposits was measured along the center line of the flume using a SeaTek 5 MHz Ultrasonic Ranging System (URS), comprising 16 transducers that were spaced apart by 16.2 mm. The URS calculates the vertical distance to the deposit by means of the two-way travel time of an ultrasound pulse. The housing array of the transducers was arranged parallel to the direction of flow and was moved 0.122 m downstream between individual readings, thus producing a profile with a data point every 8.1 mm along the deposit. A blank scan of the bottom of the flume was subtracted from the bed profile to determine deposit thicknesses. The runout distance of each deposit, defined as the distance the flow travelled from the lock gate before coming to a halt, was recorded for all flows that stopped before reaching the end of the flume. A hypothetical runout distance was determined for the flows that reflected from the far end of the flume, as explained in the dimensional-analysis section below.

The rheological characteristics of sediment mixtures with the same composition as the suspensions used in the lock-exchange experiments were measured using the Anton Paar Physica MCR 301 rheometer at IFREMER (Brest, France). These experiments were carried out at 20°C with a concentric-cylinder geometry using kaolinite suspensions at $5\% \leq C \leq 29\%$ and bentonite suspensions at $5\% \leq C \leq 20\%$. The rheological data for the silica-flour suspensions and the 1% clay suspensions are not presented herein because particle settling changed the properties of the suspensions over the course of the rheometric tests. Each experiment used 200 cm^3 samples, prepared by weighing Menai Strait seawater and clay in a plastic bottle at the desired concentration. The bottle was then manually shaken for 10 minutes to produce a homogeneous suspension. The sample was shaken for an additional 30 seconds immediately before a subsample of the suspension was added to the rheometer cup to account for any settling that may take place at low clay concentrations. Time dependencies of the rheological parameters were tested and found to be insignificant over a period of up to 12 hours and thus negligible within the typical experimental time frame of 75 minutes. The rheometer measured the rheological behavior of the suspensions, from which the yield stress was derived to give an approximation of the strength of the cohesive bonds between the clay particles. Yield-stress values obtained from the oscillatory test are presented in Table 2. This method applies a progressively increasing oscillating strain to the sediment and measures the resultant stress (van Vliet 2013). The trend between yield stress and clay concentration derived from the oscillatory tests was found to agree well with that of strain- and stress-controlled tests also conducted for both clay types.

EXPERIMENTAL RESULTS

The behavior of the experimental SGFs varied notably with the initial suspended-sediment concentration and the type of sediment. Below,

TABLE 2.—Experimental data. TC, turbidity current.

Run Number	Sediment Type	Initial Sediment Concentration C (vol %)	Run-Out Distance (m)	Maximum Head Velocity (m s^{-1})	Yield Stress (N m^{-2})	Flow Type
1	Silica flour	1	-	0.11	-	Low-density TC
2	Silica flour	5	-	0.24	-	Low-density TC
3	Silica flour	10	-	0.34	-	Low-density TC
4	Silica flour	15	-	0.45	-	Low-density TC
5	Silica flour	25	-	0.58	-	Low-density TC
6	Silica flour	40	-	0.69	-	Low-density TC
7	Silica flour	44	-	0.71	-	Low-density TC
8	Silica flour	46	-	0.75	-	High-density TC
9	Silica flour	47	4.66	0.75	-	High-density TC
10	Silica flour	48	3.68	0.71	-	High-density TC
11	Silica flour	49	2.82	0.71	-	High-density TC
12	Silica flour	50	1.53	0.64	-	High-density TC
13	Silica flour	51	0.96	0.61	-	Mud flow
14	Silica flour	52	0.49	0.29	-	Slide
15	Kaolinite	1	-	0.11	-	Low-density TC
16	Kaolinite	5	-	0.28	0.34	Low-density TC
17	Kaolinite	10	-	0.33	8.77	Low-density TC
18	Kaolinite	15	-	0.41	15.5	Low-density TC
19	Kaolinite	22	4.35	0.50	41.2	High-density TC
20	Kaolinite	23	3.66	0.48	-	High-density TC
21	Kaolinite	25	2.09	0.48	67.2	High-density TC
22	Kaolinite	27	1.01	0.40	93.8	Mud flow
23	Kaolinite	29	0.45	0.29	141.2	Slide
24	Bentonite	1	-	0.10	-	Low-density TC
25	Bentonite	5	-	0.23	0.77	Low-density TC
26	Bentonite	10	-	0.31	7.35	Low-density TC
27	Bentonite	15	4.66	0.35	21.7	High-density TC
28	Bentonite	16	3.77	0.37	28.9	High-density TC
29	Bentonite	17	3.12	0.34	34.7	High-density TC
30	Bentonite	18	1.42	0.27	37.0	Mud flow
31	Bentonite	19	1.22	0.22	119.0	Mud flow
32	Bentonite	20	0.22	0.07	217.3	Slide

observed differences in the shape and kinematic behavior of the head of the flows, and spatial trends in their head velocity and deposit thickness, are described for the noncohesive silica flour, the weakly cohesive kaolinite, and the strongly cohesive bentonite. The focus is on the heads of the SGFs, but the background-video data suggest that the head behavior is representative of the body behavior of the flows. Table 2 summarizes the main experimental data.

Silica-Flour Flows

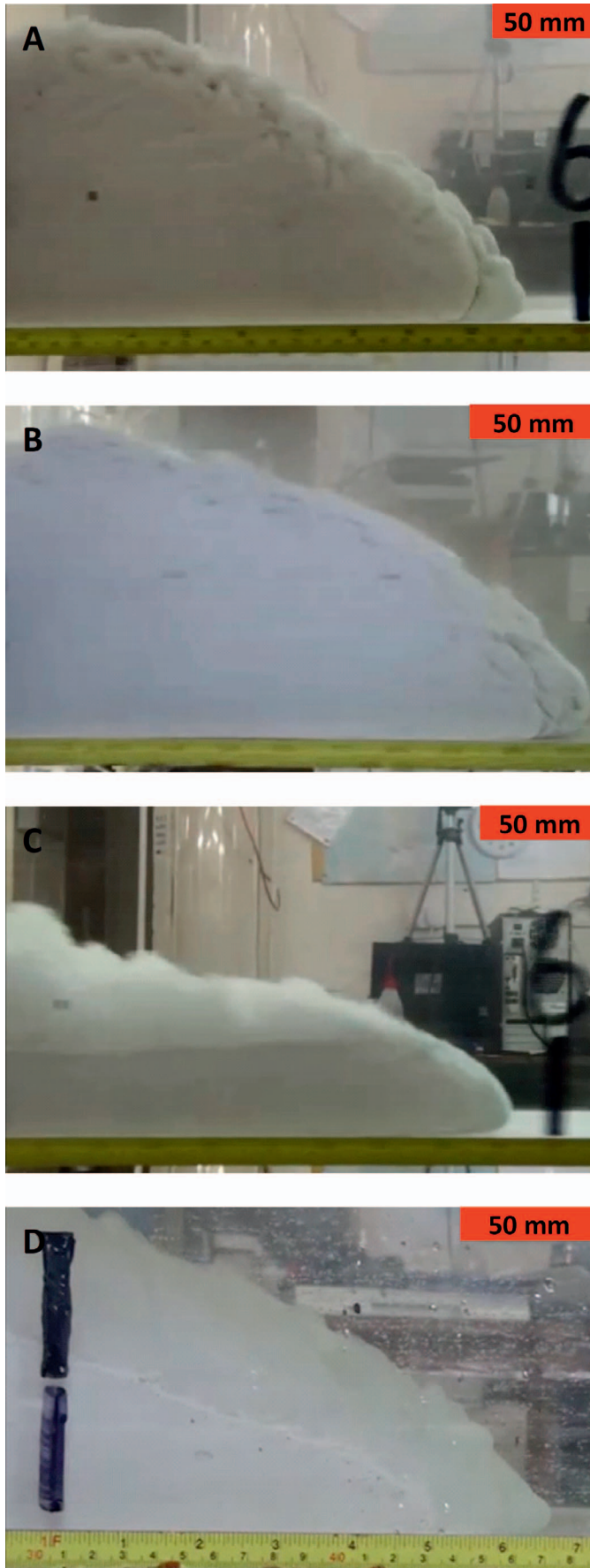
Visual Observations.—Video recordings of the silica-flour-laden flows show marked changes in the behavior of the heads of these flows, as the initial suspended-sediment concentration, C , was increased from 1% to 52%. Along the entire length of the flume, the flows that carried up to 44% silica flour were visually dominated by turbulent mixing, both within the head and body and at their boundaries (Figs. 2A, B). On leaving the reservoir, these flows developed a pointed semi-elliptically-shaped head with a prominent nose in the flow-parallel vertical section. This shape, as well as the thickness of the head of these flows, remained constant along the flume. The height of the body fluctuated owing to the development of Kelvin-Helmholtz instabilities at the upper surface of the flows.

The flows that carried between 46% and 50% silica flour comprised two zones: a lower zone 1 without visible internal mixing and an upper zone 2 where ambient water was mixed into the flow (Fig. 2C). The boundary between these zones was well defined by a vertical change in color (Fig. 2C). This color contrast increased from $C=46\%$ to $C=50\%$. The heads of the 46% to 48% silica-flour flows showed a semi-elliptical shape similar to

the $C < 46\%$ flows. However, the nose gradually became more rounded, as the concentration increased. At $C \geq 49\%$, the shape of the head of the flows was rounded with a blunter nose than at lower C values. At $C \geq 47\%$, the flows stopped before reaching the end of the tank, but sediment from the dilute upper zone of the flow continued to travel along the length of the flume.

The $C = 51\%$ and $C = 52\%$ flows were poorly mixed internally and exhibited only minor mixing with ambient water (Fig. 2D). Instead, the ambient water was swept over the front and the top of the flows. The 52% flow was wedge-shaped, rendering it difficult to distinguish the head from the body of this flow. A dilute cloud of silica flour developed above the flows with $C = 51\%$ and $C = 52\%$ (Fig. 2D). This cloud travelled slowly down the length of the flume after the main flow had stopped.

Flow Velocities.—Figure 3A and B shows that each SGF increased in velocity rapidly once the gate was lifted, reaching a maximum head velocity, U_h , that increased from 0.11 m s^{-1} to 0.75 m s^{-1} , as the suspended-sediment concentration of the flows was increased from 1% to 47%. At $C \geq 48\%$, U_h decreased progressively from 0.71 m s^{-1} to 0.29 m s^{-1} (Table 2). After the initial increase, the head velocity of all flows decreased along the remainder of the flow path. However, higher-frequency fluctuations were superimposed on this trend of reducing head velocity, especially in the denser flows. The maximum recorded fluctuation in head velocity was $c. 0.2 \text{ m s}^{-1}$ in the 46% flow (Fig. 3B), which is 27% of the maximum head velocity. Within the limits of the flume, the flows with $C \leq 25\%$ showed a gradual spatial decrease in head velocity, while the $C = 40\%$



to $C = 46\%$ flows exhibited a greater rate of decrease in the final flow stages, in addition to this gradual decrease. The flows with $C \geq 47\%$ also displayed a rapid decrease in velocity in the final stages, but the velocity decreased to zero before these flows reached the end of the flume. As the initial silica-flour concentration was increased from 47% to 52%, the maximum distance of travel of these flows progressively shortened (Fig. 3B, Table 2).

Deposits.—All the flows with $C \geq 47\%$ produced a measurable runoff distance (Fig. 4), translating into deposit lengths that decreased from 4.66 m to 0.49 m as C was increased from 47% to 52% (Table 2). These deposits were thickest at the back of the reservoir, where also the maximum thickness increased with increasing flow density (Fig. 4). The deposits of the 47% to 49% flows decreased steadily in thickness from the back of the reservoir to a horizontal distance from the lock gate, x , of 1.1 m, attaining a constant thickness thereafter. The termination of the deposit of the 47% flow was wedge-shaped, whereas the deposits of the 48% and 49% flows had abrupt terminations (Fig. 4). The 50% and 51% flows produced deposits that thinned from the back of the reservoir to $x = 0.83$ m and $x = 0.65$ m, respectively, before increasing in thickness again, thus exhibiting a distinct depression in the deposits. As with the 48% and 49% flows, the deposits of the 50% and 51% flows ended abruptly. The flow that carried 52% silica flour did not produce a depression in its deposit. Instead, this deposit dipped steeply and almost uniformly from the back of the reservoir to $x = 0.49$ m (Fig. 4).

Kaolinite and Bentonite Flows

Visual Observations.—The bentonite flows of $C \leq 10\%$ and the kaolinite flows of $C \leq 15\%$ behaved in a manner similar to that of the low-concentration silica-flour flows (Fig. 5A), thus exhibiting strong turbulent mixing, both internally and at flow boundaries, pointed semi-elliptically shaped heads with a pronounced nose, and Kelvin-Helmholtz instabilities at the upper boundary.

The 22%, 23%, and 25% kaolinite flows and the 15% and 16% bentonite flows consisted of a dark lower zone 1, overlain by an upper zone 2 with a lighter shade, where ambient water mixed into the flow (Fig. 5B, E). These zones were separated by interfacial waves in the 15% and 16% bentonite flows. These waves were particularly prominent in the final flow stages of the 15% bentonite flow. Coherent fluid-entrainment structures (CFESs), expressed as linear features of clear ambient water along the side wall of the flume, were present in zone 1 of the head of the 22% and 23% kaolinite flows until the final flow stages. CFESs also developed in zone 1 of the 15% and 16% bentonite flows, but these features were visible only in the midsection of the 15% bentonite flow. In the 16% bentonite flow, a long quasi-horizontal CFES developed at $x \approx 0.60$ m, above which multiple angled CFESs were present (Fig. 5E). This layer of CFESs moved on top of a dense, featureless layer to $x \approx 3$ m, after which the entire dense zone 1 became featureless. The videos revealed packets of cohesive sediment in the head of the 15% bentonite flow and more frequently in the 16% flow (Fig. 5E). Occasionally, these packets were pushed over the top of the head before disintegrating or carried along at the floor of the flume before being incorporated into the head of the flow (Fig. 5E).

The head of the 17% bentonite flow had a three-part signature: (i) a dense lower zone 1a, which contained horizontal sheets of water; (ii) a

←

FIG. 2.—Video snapshots of the heads of the silica-flour flows at **A**) $C = 5\%$, where the flow was fully turbulent, at $t = 8.00$ s and at $x = 1.80$ m along the tank; **B**) $C = 25\%$, which was also turbulence-dominated, at $t = 1.70$ s and $x = 0.90$ m; **C**) $C = 48\%$, showing a two-layer HDTC structure, at $t = 3.40$ s and $x = 1.80$ m; **D**) $C = 52\%$, a slide in its final stages, at $t = 5.87$ s and $x = 0.43$ m.

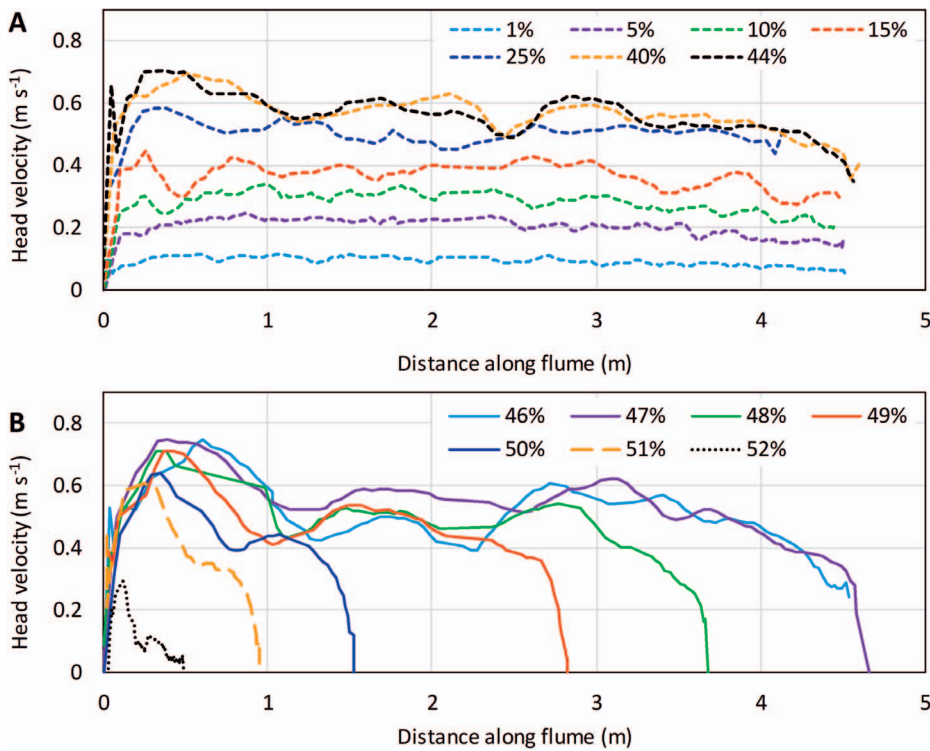


FIG. 3.—Changes in the head velocity of the silica-flour flows with **A**) $1\% \leq C \leq 44\%$, and **B**) $46\% \leq C \leq 52\%$, along the length of the lock-exchange tank. The short-dashed, continuous, long-dashed, and dotted lines indicate low-density turbidity currents, high-density turbidity currents, mud flow, and slide, respectively.

middle zone 1b with active mixing and CFESs; and (iii) a dilute upper zone 2, dominated by mixing with the ambient water (Fig. 5F). This three-part structure was visible from $x = 1.05$ m to $x = 2.43$ m, after which the CFESs reached the base of the flow, producing a two-part structure. From 1.32 m, the head of the $C = 22\%$ kaolinite flow could be divided into the same three-part structure as the $C = 17\%$ bentonite flow, although zone 1a was featureless. This three-part structure was visible until $x = 3.30$ m, after which zone 1b and the CFESs ceased to exist.

The $22\% \leq C \leq 25\%$ kaolinite flows and the 15% and 16% bentonite flows had a pointed semi-elliptical head with a prominent nose, and all experienced hydroplaning (Fig. 5B, E). However, from $x = 0.41$ m to $x = 1.35$ m the head of the 25% kaolinite flow attained a rounded semi-ellipse shape, as sediment was thrown over the top of the head (Fig. 5B). The head of the hydroplaning 17% bentonite flow was semicircular (Fig. 5F).

The head of the 18% and 19% bentonite flows and the 27% kaolinite flow lacked any noticeable internal turbulence and mixing with the ambient water, but a dilute suspension cloud developed at the front of the bentonite flows (Fig. 5C, G). The 27% kaolinite flow had a pointed, wedged-shaped hydroplaning head which produced an extremely weak suspension cloud as it travelled along the tank (Fig. 5C). The shape of the heads of the flows that carried 18% and 19% bentonite were unique compared with all other flows. Upon leaving the reservoir, the heads of these flows lifted off the base of the flume and folded back on themselves, thus attaining a distinct and persistent roller-wave-like shape (Fig. 5G). During the final flow stages, the fold at the top of the head dropped back towards the floor of the flume, resulting in a blunt semicircular frontal shape. Both the 27% kaolinite and 19% bentonite flows developed vertical tension cracks (< 10 mm deep) oriented perpendicular to the side wall of the flume (Fig. 5C).

The highest-concentration kaolinite and bentonite flows, at $C = 29\%$ and $C = 20\%$ respectively, travelled out of the reservoir as coherent masses that neither mixed with the ambient water nor hydroplaned. The 29% kaolinite suspension produced a flow with a blunt, rounded head and a steeply inclined body (Fig. 5D). The 20% bentonite flow lacked a clearly defined head (Fig. 5H). However, minor folds developed in the front of the flow

and tension cracks were present length-parallel to the flow direction in the two lowest folds.

Flow Velocities.—The head velocity of all the kaolinite and bentonite flows increased rapidly as the flows left the reservoir, after which the head velocity decreased as the flows travelled farther down the flume (Figs. 6, 7). The U_h of the bentonite flows increased from 0.10 m s⁻¹ for $C = 1\%$ to 0.37 m s⁻¹ for $C = 16\%$, and then decreased to 0.07 m s⁻¹ for $C = 20\%$. In comparison, the U_h of the kaolinite flows increased from 0.11 m s⁻¹ for $C = 1\%$ to 0.50 m s⁻¹ for $C = 22\%$, and then decreased to 0.29 m s⁻¹ for $C = 29\%$ (Table 2). The flows with $C \geq 22\%$ kaolinite and $C \geq 15\%$ bentonite stopped before reaching the end of the flume, owing to a rapid decrease in velocity in the final flow phase (Figs. 6, 7). This phase of rapidly decreasing velocity occurred progressively closer to the lock gate, as the C values were increased above 15% bentonite and 22% kaolinite (Fig. 6B, 7B). As in the silica-flour flows, all the clay flows exhibited velocity fluctuations superimposed on a longer trend of slowing flow. These fluctuations reached a maximum of $c. 0.1$ m s⁻¹ in the 15% bentonite and kaolinite flows, which corresponds to 29% and 24% of U_h , respectively. The 29% kaolinite flow behaved somewhat differently, in that, after an initial decrease in velocity from 0.3 m s⁻¹ to 0.01 m s⁻¹, the flow continued to move forward at 0.01 m s⁻¹ for 0.33 m before stopping (Fig. 6B).

Deposits.—The flows with $C \geq 22\%$ kaolinite and $C \geq 15\%$ bentonite produced measurable runout distances in the 4.69-m-long tank (Figs. 8, 9). The deposits decreased in length from 4.66 m for 15% bentonite to 0.22 m for 20% bentonite, and from 4.35 m for 22% kaolinite to 0.46 m for 29% kaolinite. All the clay flow deposits were thickest near the back of the reservoir. The $15\% \leq C \leq 17\%$ bentonite flows and the 22% and 23% kaolinite flows thinned steadily from the back of the reservoir to $x \approx 1$ m; thereafter, the bed thickness remained constant until the deposits ended with a pronounced leading edge (Figs. 8, 9). The deposits of the 18% and 19% bentonite flows and the 25% and 27% kaolinite flows consisted of distinct depressions, which were 0.03–0.04 m deep at $x \approx 0.60$ m for the

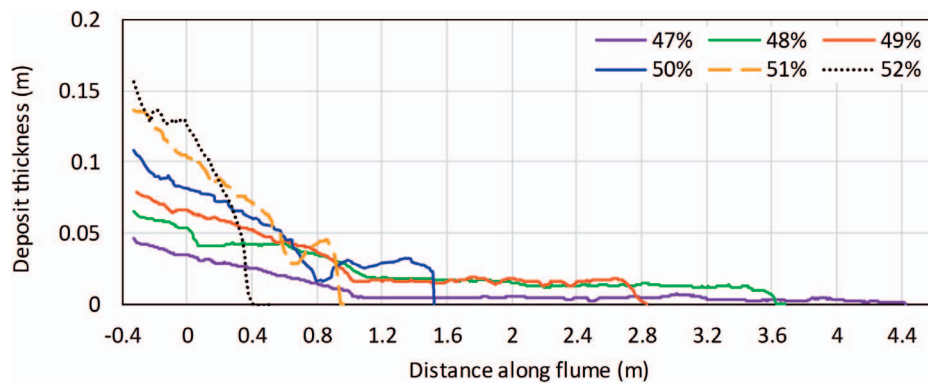


FIG. 4.—Deposit thickness against distance along the tank for all silica-flour flows with measurable runout distance. See Figure 3 for explanation of line styles.

bentonite flows (Fig. 9). The depression in the deposit of the 25% kaolinite flow reached the floor of the flume at $x = 0.71$ m, whereas 0.016 m of sediment was deposited in the depression of the deposit of the 27% kaolinite flow at $x = 0.50$ m (Fig. 8). The flows laden with 29% kaolinite and 20% bentonite produced deposits which decreased rapidly from their maximum thickness to zero over a distance of 0.1 m for the bentonite flow and 0.5 m for the kaolinite flow to produce block-shaped and wedge-shaped deposits, respectively (Figs. 8, 9).

Comparison of Maximum Head Velocities and Runout Distances

Figure 10 compares the maximum head velocities and runout distances for the three sediment types as a function of initial suspended-sediment concentration. Up to $C = 10\%$, U_h increased at a similar rate for these sediment types (Fig. 10A). As suspended-sediment concentration was increased further, U_h started to diverge, e.g., attaining 0.35 m s^{-1} for bentonite, 0.41 m s^{-1} for kaolinite, and 0.45 m s^{-1} for silica flour at $C = 15\%$. The bentonite flows achieved the highest U_h at $C = 16\%$. With a further increase in bentonite concentration, U_h decreased rapidly until the bentonite was no longer able to flow out of the reservoir at an estimated $C \approx 20.5\%$ (Fig. 10A). The $C-U_h$ curves for the bentonite, kaolinite, and silica-flour flows have a similar shape, but the maximum U_h and the suspended concentrations at which this maximum velocity was reached, were significantly higher for kaolinite and silica flour. The kaolinite flows reached $U_h = 0.50 \text{ m s}^{-1}$ at $C = 22\%$, and the silica-flour flows attained $U_h = 0.75 \text{ m s}^{-1}$ at $C = 47\%$ (Fig. 10A). The kaolinite and silica-flour suspensions failed to leave the reservoir at estimated C values of 30.5% and 53%, respectively.

Within the confinement of the flume, the runout distance of the SGFs strongly depended on concentration and clay type (Fig. 10B). Progressively less suspended sediment was required to produce a deposit of comparable length for silica flour, kaolinite, and bentonite. For example, the 19% bentonite flow had a runout distance of 1.22 m, whereas 27% of kaolinite and 51% of silica flour were needed to achieve a similar runout distance. 15% bentonite was required to produce deposits that were limited in length to the confinement of the flume (i.e., $x \leq 4.69$ m). This threshold concentration was much higher for kaolinite, at $C = 22\%$, and for silica flour, at $C = 47\%$ (Fig. 10B).

PROCESS INTERPRETATIONS

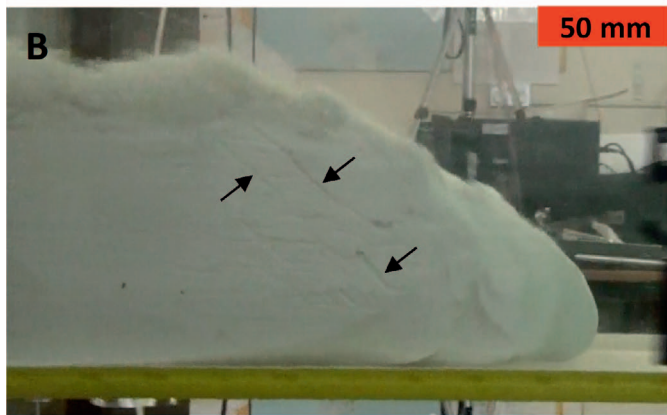
Silica-Flour Flows

Silica flour is composed of ground quartz and is generally assumed to be noncohesive (Parker et al. 1987; Baas et al. 2005; Felix and Peakall 2006; Kane et al. 2010). However, Pashley and Karaman (2004) found that silica-flour particles may have a weak negative surface charge owing to the disassociation in water of some of the silanol (SiOH) groups, thus

rendering silica flour weakly cohesive. These weak to noncohesive properties may have caused the silica-flour flows in this study to behave differently from the stronger cohesive kaolinite and bentonite flows, particularly at high C values. However, frictional interaction between grains, dispersive pressure, and hindered settling may have also controlled the flow behavior of the silica-flour suspensions, as discussed below.

Visual Observations.—The flows laden with $C \leq 44\%$ silica flour behaved in a manner similar to that of experimental turbidity currents in other studies (Fig. 2A, B; e.g., Kuenen and Migliorini 1950; Middleton 1966; Marr et al. 2001); they were fully turbulent, thus allowing the sediment particles to be supported by the upward velocity component of fluid turbulence (Middleton and Hampton 1973; Kneller and Buckee 2000). This behavior renders these flows low-density turbidity currents (LDTC; Table 3), following the definition of Lowe (1982). These flows remained fast-moving with pronounced Kelvin-Helmholtz instabilities at the upper boundary up to $C = 44\%$, owing to the large density difference with the ambient water and the small particle size ($D_{50} = 18.2 \text{ }\mu\text{m}$). Consequently, turbulent energy in the flows was able to outcompete the particle settling velocity, and keep the particles in suspension. High dispersive pressure and hindered settling may also have helped the particles remain suspended (Middleton and Hampton 1973).

The $46\% \leq C \leq 50\%$ silica-flour flows were classified as high-density turbidity currents (HDTC; *sensu* Lowe 1982; Table 3), as these flows comprised a dense lower zone 1 separated from a dilute upper zone 2 by a break in density (Fig. 2C). Zone 1 formed from the accumulation of particles near the base of the flow, and zone 2 resulted from shear-induced mixing of sediment with the ambient water. The $C = 51\%$ silica-flour flow is classified as a noncohesive mud flow (NCMF) due to its strong to full turbulence suppression and limited mixing at the upper boundary (Table 3). Finally, the $C = 52\%$ silica-flour flow is classified as a slide, following the definition of a high-density SGF that moves as a coherent mass without significant internal deformation (Fig. 2D; Table 3; Martinsen 1994; Mohrig and Marr 2003). At $C \geq 48\%$ the flow mobility decreased progressively, and the flow density approached the cubic-packing density of clastic sediment (*c.* 52%). It is therefore inferred that frictional interactions between particles prevented the development of turbulence in these flows, thus outcompeting the effect of excess density, encouraging bulk settling and slowing down the flows (Iverson 1997). The flows with $C \geq 47\%$ showed a dilute suspension cloud that outran the main body of the flow (Fig. 2D). While the dense main body of the 47% to 50% HDTCs slowed and stopped, as the frictional forces outcompeted the excess density, the dilute suspension cloud was driven by turbulence and still had enough momentum to continue flowing. Minor erosion at the top of the 51% and 52% silica-flour flows helped in producing the dilute turbidity current, which was then able to travel slowly along the entire length of the tank.



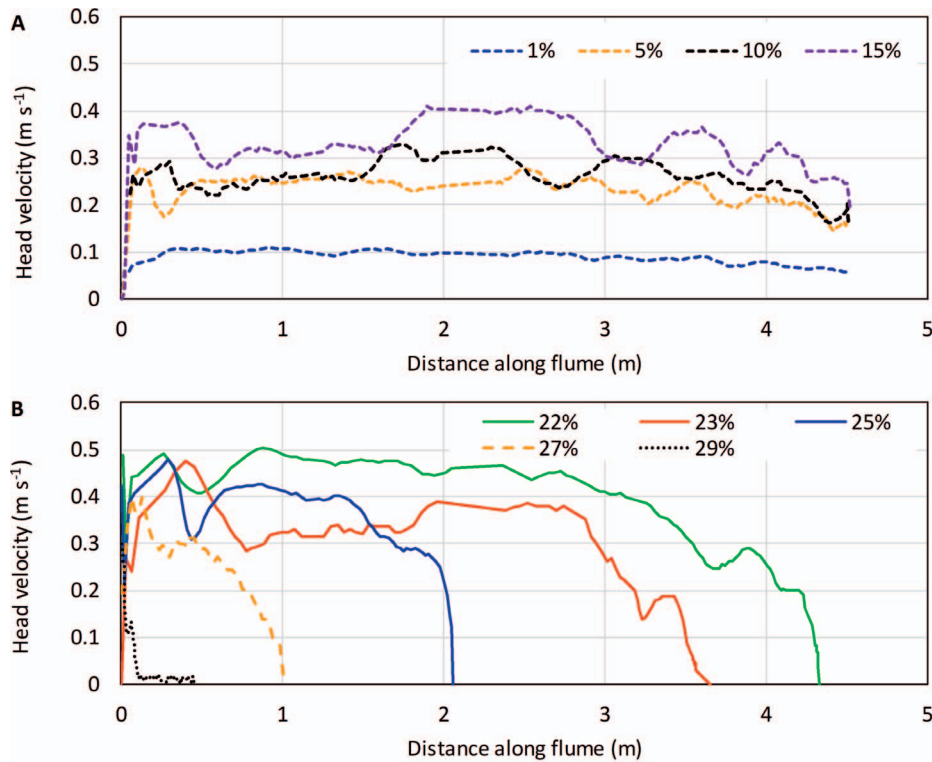


FIG. 6.—Changes in the head velocity of the kaolinite flows with **A)** $1\% \leq C \leq 15\%$, and **B)** $22\% \leq C \leq 29\%$, along the length of the lock-exchange tank. See Figure 3 for explanation of line styles.

In contrast to the kaolinite and bentonite flows herein and other high-density clay-laden SGFs described in the literature (Fig. 2; Marr et al. 2001; Elverhøi et al. 2005), none of the silica-flour flows hydroplaned. Hydroplaning occurs when the dynamic pressure generated in the ambient fluid just below the head of the flow approaches or exceeds the weight per unit area of the material in the head of the flow (Mohrig et al. 1998). Another requirement for hydroplaning is that the permeability of the base of the flow is low enough to prevent mixing of the overridden water into the flow above (Talling 2013). This permeability requirement may not have been achievable for the silica-flour flows because of the lack of cohesive strength in these flows. In the LDTCs and HDTCs in particular, the high turbulent energy and small particle size meant that any water forced underneath the head was rapidly mixed into the flow. The NCMF and slide may have had a permeable base as well, but these dense flows were probably also too heavy and did not travel quickly enough to allow water to be forced underneath the head of the flow.

The pointed semi-elliptical shape of the head of the silica-flour flows with $C \leq 48\%$ is commonly seen in turbidity currents of relatively low density and low internal strength, in which the head is shaped into a streamlined form to minimize the pressure force at the front of the flow (Fig. 2A–C; Hampton 1972; Middleton 1993). Although the 46% and 48% flows behaved as HDTCs, the heads of these flows apparently did not have enough internal strength to resist being shaped by the hydrodynamic pressures (Britter and Simpson 1978; Kneller and Buckee 2000). Only the

silica-flour flows with $C \geq 49\%$ had enough internal strength to produce rounded-shaped heads. This strength may result from a variety of mechanisms: high dispersive pressure, hindered settling, frictional interaction between grains, and weak negative surface charge of silica flour (Middleton and Hampton 1973; Iverson 1997; Pashley and Karaman 2004). The flows with $C \geq 49\%$ also had relatively low head velocities, which reduced the hydrodynamic pressure on the heads of these flows, and thus the ability to streamline the head (Mohrig et al. 1998).

Flow Velocities.—The silica-flour flows reached a progressively higher maximum head velocity as the initial suspended-sediment concentration was increased from 1% to 47%, because increasing the concentration increased the density difference between the sediment suspension and the ambient fluid, and it is this difference that drives the flow. However, increasing C above 47% reduced the maximum velocity to which the flows accelerated, which is interpreted as a further expression of the effect of friction between the sediment grains on the mobility of these high-concentration flows, mentioned above.

The rate of decrease of the head velocity of the silica-flour-laden flows increased as C was increased. At $C \leq 25\%$, the head velocity decreased relatively slowly, driven by resistive shear forces, along the length of the tank (Fig. 3A; Kneller and Buckee 2000). At higher concentrations, the flows slowed more quickly, especially at $C \geq 47\%$, where all the flows showed a rapid spatial decrease to zero velocity (Fig. 3B; cf. Hallworth and Huppert

FIG. 5.—**A)** Head of the turbulent 5% kaolinite LDTc at $t = 6.60$ s and $x = 1.49$ m. **B)** Head of the 22% kaolinite flow at $t = 3.50$ s and $x = 1.50$ m; this HDTc hydroplaned and was divided into three parts; the arrows highlight the CFESs. **C)** Pointed head of the kaolinite mud flow with $C = 27\%$ at $t = 3.50$ s and $x = 0.89$ m; small tension cracks, shown by the arrows, are visible on the top of the head of the flow. **D)** Rounded head of the kaolinite slide with $C = 29\%$ at $t = 2.50$ s and $x = 0.35$ m. **E)** Tripartite head of the 16% bentonite flow at $t = 6.07$ s and $x = 1.77$ m; a cohesive packet of clay is visible at the base of the head of this HDTc, shown by lower arrow; the upper arrow highlights a CFES. **F)** Head of the 17% bentonite flow at $t = 5.40$ s and $x = 1.49$ m; the horizontal sheets and angled CFESs are shown by the arrows. **G)** Mud flow laden with 19% bentonite, showing a folded head, at $t = 2.73$ s and $x = 0.56$ m. **H)** Front of the $C = 20\%$ bentonite slide at $t = 5.43$ s and $x = 0.13$ m.

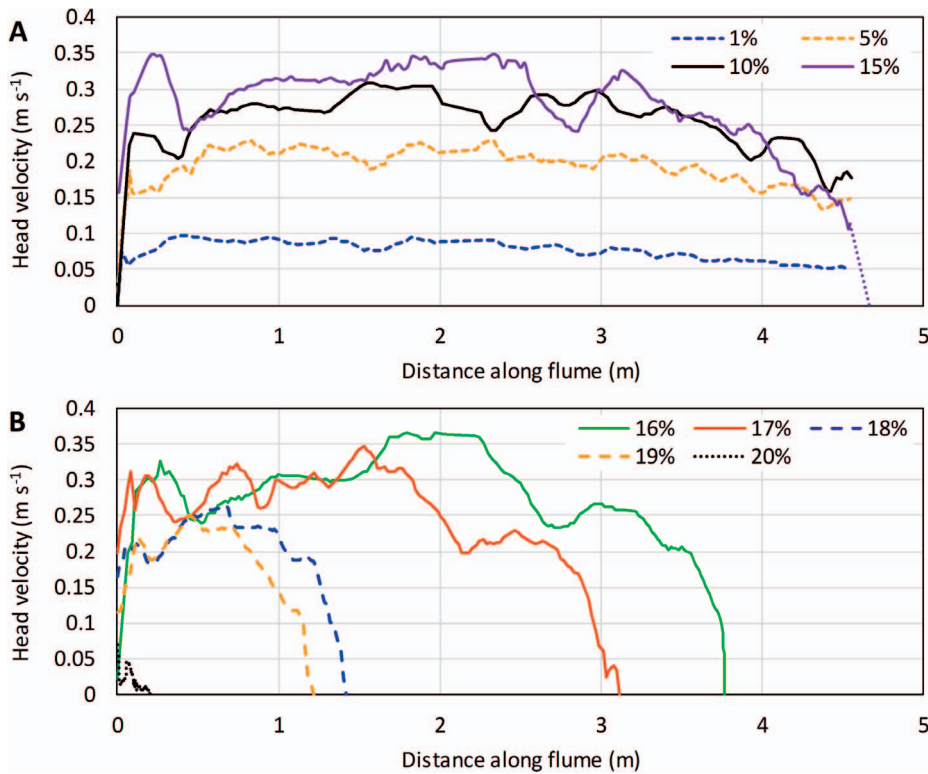


FIG. 7.—Changes in the head velocity of the bentonite flows with A) $1\% \leq C \leq 15\%$, and B) $16\% \leq C \leq 20\%$, along the length of the lock-exchange tank. See Figure 3 for explanation of line styles. Purple dotted line in Part A denotes extrapolated velocity to the recorded runoff distance.

1998). This process is attributed to frictional freezing (Mutti et al. 1999; Mulder and Alexander 2001; Kane et al. 2009). As the flow starts to slow down, the vertical settling velocity of the grains becomes greater than the horizontal movement, and the flow contracts vertically. This contraction process brings the particles into closer proximity, resulting in greater frictional forces, which further reduce the forward momentum of the particles. This positive feedback thus leads to a rapid decline in head velocity. The origin of the velocity fluctuations superimposed on the general trend of slowing head velocity is unclear. These fluctuations might be attributable to the formation of elongate packets of sediment with contrasting velocity within lobes and clefts at the base of the flow, and interaction of the flow with waves on the water surface, produced by the displacement of ambient water upon release of the suspension from the reservoir.

Deposits.—All flows of $C \geq 47\%$ silica flour produced a measurable runoff distance which decreased in length as the suspended-sediment

concentration increased, because frictional freezing occurred closer to the point of release (Figs. 3B, 4). The HDTCs, NCMF, and slide with $C \geq 47\%$ deposited all or most of the silica flour within $c. 1$ m of the lock gate, forming steeply inclined, wedge-shaped sediment bodies (Fig. 4). This is further testament to the dominance of frictional forces over turbulent forces at these high suspended-sediment concentrations. However, part of the sediment in the HDTCs was transported beyond $x = 1$ m, suggesting that the remaining turbulent forces were able to keep part of the silica flour in suspension until frictional freezing commenced. The blocky shape of these deposits agrees well with the shape of deposits formed by high-density SGFs in the Marnoso-arenacea Formation, Italy (Amy et al. 2005, their Fig. 3B). The depression in the deposits of the 50% and 51% flows (Fig. 4) resembles those that Elverhøi et al. (2005) associated with flow “stretching” due to hydroplaning, which causes the head of a dense flow to accelerate away from the body. However, the silica-flour flows in the present study did not hydroplane, suggesting that other mechanisms may also create these depressions. Internal velocity measurements are needed to

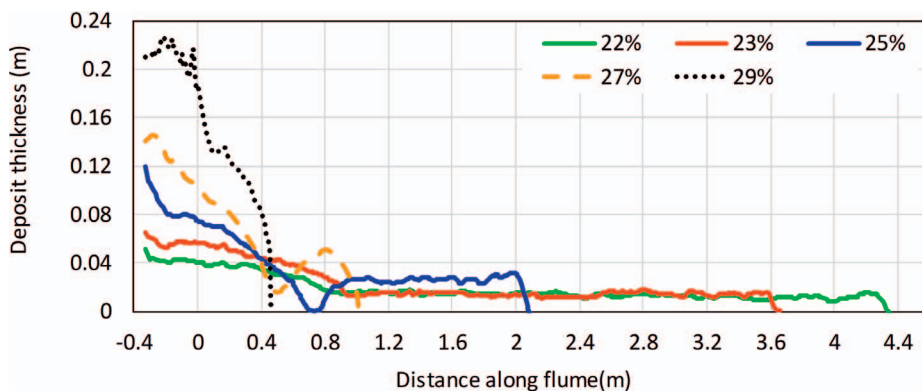


FIG. 8.—Deposit thickness against distance along the tank for all kaolinite flows with measurable runoff distance. See Figure 3 for explanation of line styles.

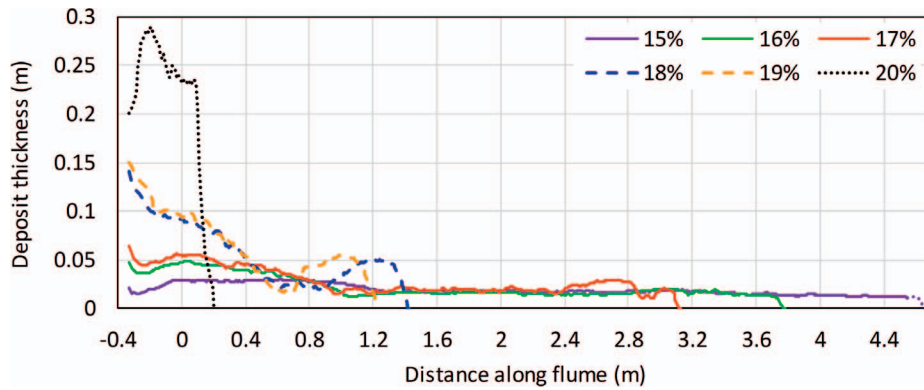


FIG. 9.—Deposit thickness against distance along the tank for all bentonite flows with measurable runoff distance. See Figure 3 for explanation of line styles. Dotted end of the deposit for the 15% flow was beyond the reach of the SEATEK ranging system, and was measured by hand instead.

ascertain how these features form in non-hydroplaning flows. The 52% flow did not produce a deposit with a depression, possibly because of a lack of internal velocity gradients, which is typical for a slide moving as a rigid plug.

Kaolinite and Bentonite Flows

Visual Observations.—The kaolinite and bentonite flows of $C \leq 15\%$ and $C \leq 10\%$, respectively, behaved as LDTCs (Table 3), with a streamlined semi-elliptically shaped head and fully dominated by turbulent mixing in the head and body (Middleton 1966; Middleton and Hampton 1973; Lowe 1982; Sumner et al. 2009). The flows that carried between 22% and 25% kaolinite and between 15% and 17% bentonite showed HDTC behavior, where a typically distinct color difference between the dense zone 1 and the dilute zone 2 and the presence of interfacial waves suggest the presence of a break in density (Table 3; Fig. 5B, E, F; Kuenen 1951; Britter and Simpson 1978; Lowe 1982; Middleton 1993; Baas et al. 2004). These clay-laden HDTCs can be classified as transitional flows (*sensu* Baas and Best 2002; Wang and Plate 1996; Kane and Pontén 2012). Herein, the high concentration of clay particles in zone 1 of these flows caused the transient-turbulent behavior. In this near-bed flow layer, the probability for particles to collide, flocculate, and form gels was high, which made the flows viscous, attain a higher cohesive strength, and thus become subjected to turbulence suppression (Baas et al. 2009; Cartigny et al. 2013). The 22% kaolinite flow and the 17% bentonite flow produced a three-part structure along part of their flow path (Fig. 5B, F). The horizontal sheets of water in the basal zone 1a of the 17% bentonite flow appeared to form by injection of water at the flow front. The formation of CFESs in zone 1b of both flows suggests that this zone had a slightly lower cohesive strength than zone 1a. The flows were probably too slow, and therefore too cohesive, to develop the three-part structure in the early and late flow stages. Instead, the two-part structure, discussed above, prevailed. Alternatively, the two-part flow structures may have remained after deposition of clay from basal zone 1a in the final flow stages (cf. Cartigny et al. 2013). Although it cannot be ruled out that the formation of the CFESs in zone 1 of the HDTCs was limited to the side wall of the flume, the presence of CFESs implies that the flows had a high enough yield stress to limit turbulent mixing of the entrained water into the flow.

The 15% and 16% bentonite flows carried packets of cohesive sediment, which formed when small sections of cohesive sediment were torn off zone 1 by ambient water forced over the front of the flows (Fig. 5E). This suggests that the shear force imposed by this ambient water at times exceeded the yield stress of the sediment suspension. These packets of bentonite were cohesive enough to resist mixing with the ambient water, as they were thrown over the top of the head. Yet, these packets were seen to disintegrate and become incorporated into dilute mixing zone 2 under the influence of high turbulence. Packets that were carried along at the base of

the head survived for longer, presumably because the shear forces at the base of zone 1 were weaker than near the top of zone 2.

The clay concentration in the flows with $C \geq 25\%$ kaolinite or $C \geq 17\%$ bentonite appeared high enough to form clay gels, i.e., pervasive, volume-filling networks of clay particle bonds, throughout the flow (Fig. 5C, D, G, H; Baas et al. 2009). These gels are inferred to have had a high enough yield stress to form rigid-plug flows without internal turbulence, typical of debris flows (Middleton and Hampton 1973; Baas et al. 2009). The 27% kaolinite flows and the 18% and 19% bentonite flows are classified herein as cohesive mud flows (CMF; Table 3). The high yield stress of these CMFs is further supported by the sharply reduced mixing with the ambient water, although the relatively weak water flow across the upper flow boundary at these high C values may also have prevented the bonds between the clay particles from breaking on a large scale. Likewise, mixing at the top of the 29% kaolinite flow and the 20% bentonite flow was negligible as a consequence of the particularly high cohesive strength and low head velocity. These flows were arrested in the sliding phase soon after the gate was lifted in a manner similar to that of the 52% silica-flour flow, and are therefore classified as slides (Table 3).

The presence of tension cracks on the tops of the 27% kaolinite flow and the 19% bentonite flow suggests that these flows were cohesive enough to have tensile strength and were placed under flow-parallel tension (Fig. 5C; Marr et al. 2001). Small spatio-temporal variations in flow velocity, partly related to hydroplaning, may have put these flows under tension. The 20%-bentonite slide exhibited tension cracks oriented parallel to the direction of slide movement. These cracks formed because the flow moved slightly faster in the center of the flume than at the sidewall, thus placing it under tension perpendicular to the flow direction.

As in the silica-flour flows, the shape of the head of the clay flows with high C values can be related to their rheological properties as well as the hydrodynamic pressure at the front of these flows (Mohrig et al. 1998). The 25% kaolinite flow attained a rounded shape for part of its flow path, the 27% kaolinite flow had a particularly thin, pointed semi-elliptically shaped head, and the 29% kaolinite flow had a blunt, semicircularly shaped head. It is inferred that these high-density flows were cohesive enough to withstand streamlining by ambient water swept over the fronts and tops of these flows (Fig. 5C, D). The roller waves in the heads of the 18% and 19% bentonite flows were particularly striking (Fig. 5G). Hampton (1972) also observed “blunt snouts with a sharp-tipped crest curled back over the top of the flow” in debris flows with a low water content (below 70% by weight). Hampton (1972) attributed this shape to the high yield stress of the flows, which allowed the water pushed back over the top of the head to create a fold that was able to resist erosion and maintain the sharp-tipped crest.

The kaolinite flows with $22\% \leq C \leq 27\%$ and the bentonite flows with $15\% \leq C \leq 19\%$ hydroplaned along parts of their flow path, thus meeting the criteria for hydroplaning discussed above (Fig. 5B, E, F, G). It is

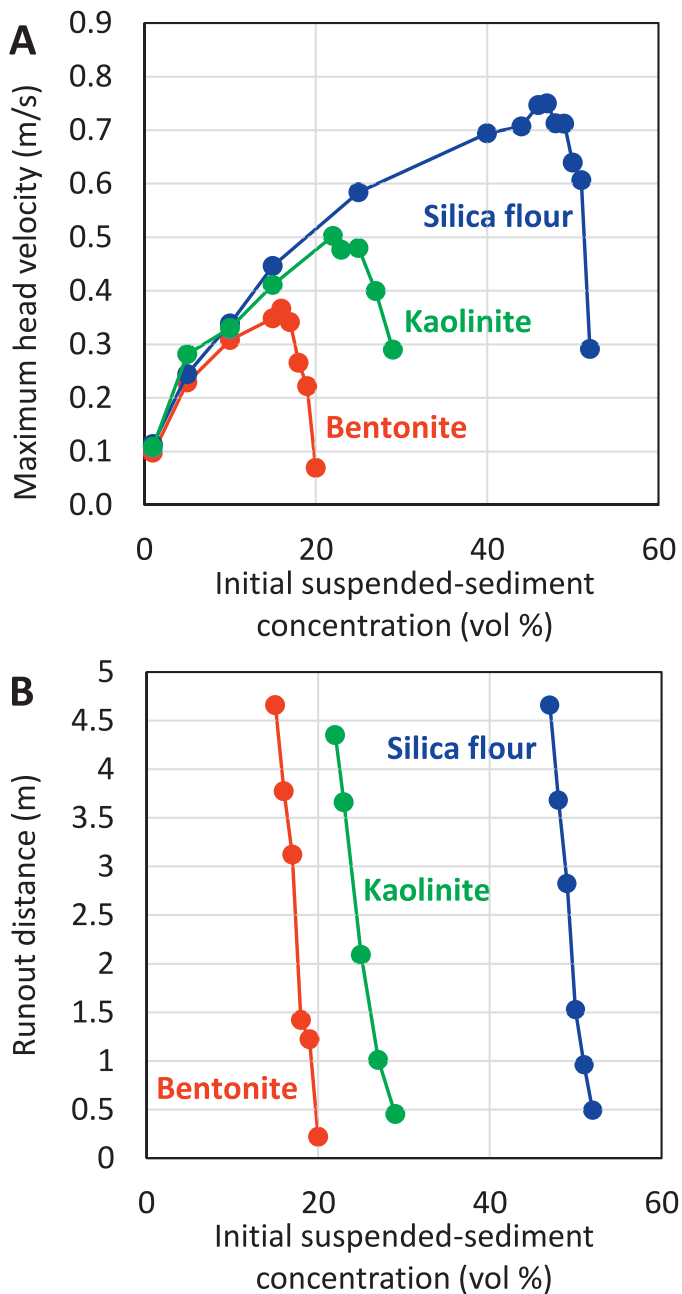


FIG. 10.—**A**) Maximum head velocity and **B**) deposit runout distance against suspended-sediment concentration for the three sediment types.

assumed that the permeability and the turbulence forces at the base of the lower-clay-concentration flows were high enough to allow water to be mixed straight into the flows. In the 29% kaolinite and 20% bentonite flows, the weight per unit area of the sediment in the head is inferred to have been too large to allow hydroplaning to develop (Fig. 5D, H). Hydroplaning did not take place either in the initial or in the final stages of the kaolinite flows with $22\% \leq C \leq 27\%$ and the bentonite flows with $15\% \leq C \leq 19\%$. Near the reservoir, the hydrodynamic pressures at the front of the head needed time to support the downward-directed weight of the flow and force a thin layer of water underneath the head (Mohrig et al. 1998; Talling 2013). As the flows slowed during their final stages, the hydrodynamic pressure at the front of the head decreased and might not

have been able to support the weight of the flows any longer, thus causing hydroplaning to end (Mohrig et al. 1998).

Flow Velocities.—The balance between turbulent forces and cohesive forces can also be used to explain the observed trends in head velocity of the clay flows (Figs. 6, 7). As in the silica-flour LDTCs, the progressive increase in head velocity with increasing concentration in the $C \leq 15\%$ kaolinite and $C \leq 10\%$ bentonite LDTCs resulted from the density difference driving these flows (Figs. 6A, 7A). We conclude that at these concentrations the cohesive forces did not influence the flow dynamics. This is further confirmed by the relatively slow decrease in the head velocity of these flows along the length of the tank, which is inferred to result from effective particle support by shear turbulence and minor particle settling (Figs. 6A, 7A).

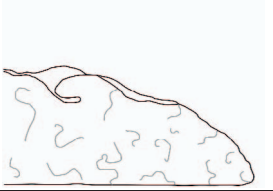
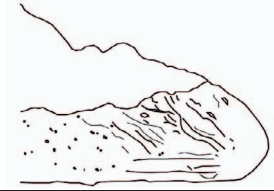
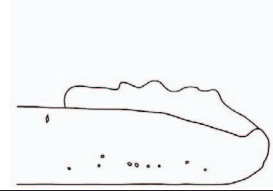
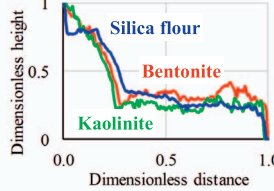
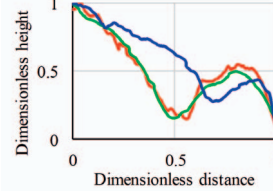
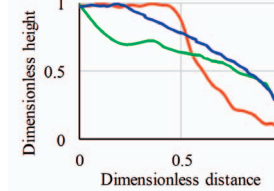
In the flows with $C > 22\%$ kaolinite and $C > 16\%$ bentonite, U_h decreased as C was increased, because the cohesive forces became stronger than the turbulent forces in these flows, despite the large density difference with the ambient water. This lack of turbulent support, combined with bulk settling of the clay gel, resulted in a rapid decrease in head velocity as the flows travelled along the tank (Figs. 6B, 7B). These flows slowed particularly quickly in the final stage, which may have resulted from “cohesive freezing” (Mulder and Alexander 2001). As the flow slows down, lower turbulent forces and flow contraction due to bulk settling allow the clay particles to form a greater number of electrostatic bonds and increase the cohesive strength of the flows. In turn, this further reduces the turbulence and encourages even greater cohesive strength. This positive-feedback mechanism allows clay flow velocities to decrease very quickly. Jacobson and Testik (2013) also produced laboratory flows composed of kaolinite with abrupt transitions, which they attributed to the presence of a lutocline, which, combined with the non-Newtonian rheology of the clay, suppressed the turbulence. As with the silica-flour flows, the high-frequency fluctuations in head velocity in the clay flows could have been related to the formation of lobes and clefts, and waves on the water surface.

Deposits.—For flows with $C \geq 15\%$ bentonite and $C \geq 22\%$ kaolinite, suspended-sediment concentration shows an inverse, linear relationship with runout distance (Figs. 8, 9). Similarly to the deposits of the silica-flour flows, the deposits of the clay flows changed from wedge-shaped with a block-shaped extension to wedge-shaped without an extension, as the flow type changed from HDTC via CMF to slide (Figs. 8, 9; Table 3). Strong cohesive forces caused rapid bulk settling of clay gels in the reservoir and down to $x = 1$ m, and turbulent forces in the HDTCs were able to move part of the clay into the flume and form block-shaped deposits with an abrupt termination associated with cohesive freezing. The deposits of the 25% and 27% kaolinite flows and the 18% and 19% bentonite flows showed distinct depressions (Figs. 8, 9; Table 3). Since all of these flows hydroplaned, the aforementioned flow-stretching mechanism of Elverhøi et al. (2005) may explain the depression. Interestingly, hydroplaning in the 25% kaolinite flow encouraged the head to detach completely from the body and form an outrunner block. This zero-thickness depression was found 1.37 m behind the front of the deposit, implying that the detached head stretched after separating from the body. The slides laden with kaolinite and bentonite had such a strong network of clay particle bonds that they flowed only a short distance from the reservoir.

Effect of Sediment Type on Maximum Head Velocity and Runout Distance

Figure 10A shows that at $C \leq 10\%$, U_h increased with increasing sediment concentration in a similar way across the three sediment types, suggesting that these flows were driven purely by the density difference. However, at $C > 10\%$, the maximum head velocities diverge, as cohesive forces in the clay flows started to attenuate turbulence. U_h kept increasing

TABLE 3.—Summary of flow and deposit properties. Dimensionless height is relative to the maximum thickness of the deposit. Dimensionless distance is relative to the runout distance.

	Low-Density Turbidity Current (LDTC)	High-Density Turbidity Current (HDTC)	Cohesive and Noncohesive Mud Flow (CMF/NCMF)	Slide
Visual flow properties	Fully turbulent; uniform color; mixing with ambient water	Dense lower layer and dilute upper layer; mixing with ambient water	Weak to no internal turbulence; some sediment entrained at top, producing dilute sediment cloud	Coherent mass without significant internal deformation
Flow shape and internal structures				
Deposit shape	Not measured, but probably elongate, thin and wedge-shaped (cf. Amy et al. 2005)			
Range of C-values	Silica flour: $C \leq 44\%$ Kaolinite: $C \leq 15\%$, Bentonite: $C \leq 10\%$	Silica flour: $46\% \leq C \leq 50\%$ Kaolinite: $22\% \leq C \leq 25\%$ Bentonite: $15\% \leq C \leq 17\%$	Silica flour: $C = 51\%$ Kaolinite: $C = 27\%$ Bentonite: $18\% \leq C \leq 19\%$	Silica flour: $C = 52\%$ Kaolinite: $C = 29\%$ Bentonite: $C = 20\%$
Yield stress boundaries	Lower boundary: 0 N m^{-2} Upper boundary: $16\text{--}22 \text{ N m}^{-2}$	Lower boundary: $16\text{--}22 \text{ N m}^{-2}$ Upper boundary: $67\text{--}94 \text{ N m}^{-2}$	Lower boundary: $67\text{--}94 \text{ N m}^{-2}$ Upper boundary: $119\text{--}141 \text{ N m}^{-2}$	Lower boundary: $119\text{--}141 \text{ N m}^{-2}$ Upper boundary: 268 N m^{-2}

decreasing rate until a maximum was reached, which is inferred to indicate the stage where flow deceleration by gelling exceeds flow acceleration by density difference. The experimental data also show that once the maximum U_h value is exceeded the cohesive forces strongly dominate, producing a rapid reduction in U_h with increasing C (Fig. 10A). The shape of the curve in Figure 10A corresponds well with the theoretical curve of velocity against clay concentration of Talling (2013). The U_h of the bentonite flows was consistently lower than that of the kaolinite flows for $C \geq 15\%$. Bentonite clay is more cohesive than kaolinite clay (Yong et al. 2012) and can therefore create a stronger network of particle bonds and resists stronger turbulent forces than kaolinite at similar C values. The silica flour also produced a convex-upward curve in Figure 10A, but frictional forces, rather than cohesive forces, started to outcompete the excess density at much higher concentrations than for kaolinite and bentonite. The same trend can be seen for the runout distances of the flows, where from silica flour via kaolinite to bentonite a progressively smaller suspended-sediment concentration is required to produce a comparable runout distance because of the contrasting rheological properties of the sediments (Fig. 10B).

TOWARDS A UNIFIED MODEL FOR HEAD VELOCITY AND RUNOUT DISTANCE

Dimensional Analysis of Maximum Head Velocity and Runout Distance

Figure 10A reveals that the bentonite, kaolinite, and silica-flour flows reacted in a similar way to changes in initial suspended-sediment concentration, driven by density difference at low C values and by cohesive and frictional forces at high C values. It should therefore be possible to describe the changes in flow behavior in terms of differences in rheological properties. Below, it is shown that the initial yield stress of the clay suspension in the reservoir can be used to delineate flow type, determine a dimensionless maximum head velocity, and determine a

runout distance largely independent of clay type. We hypothesized that the initial yield stress governs the ability of the clay suspension to leave the reservoir after lifting the lock gate. If the suspension is able to move out of the reservoir, this yield stress then controls the spatial evolution of the head velocity and the runout distance of the flow related to the conversion from potential energy to kinetic energy. Testing this hypothesis required several analytical steps: (a) nondimensionalizing the velocity curves in Figure 10A, so that the data collapse onto a single curve; (b) determining functional relationships between sediment concentration and initial-yield-stress ranges, based on the available rheometrical data for bentonite and kaolinite; (c) converting the collapsed curve for head velocity from dimensionless sediment concentration to yield stress; (d) delimiting initial yield stress ranges for LDTCs, HDTCs, CMFs, and slides; (e) establishing a functional relationship between initial yield stress and runout distance.

The maximum head velocities of the experimental bentonite, kaolinite, and silica-flour flows (Fig. 10A) were collapsed using the following best-fit equations:

$$\frac{U_h}{U_{h,m}} = \left(\frac{C}{C_m} \right)^{0.466}, \quad \text{for } 0 < C \leq C_m, \quad (1a)$$

$$\frac{U_h}{U_{h,m}} = 1 - \left(\frac{C - C_m}{C_0 - C_m} \right)^{2.82}, \quad \text{for } C_m < C \leq C_0, \quad (1b)$$

where U_h is the maximum head velocity of the flow, $U_{h,m}$ is the highest value of U_h for the sediment type under consideration (i.e., 0.75 m s^{-1} for silica flour, 0.50 m s^{-1} for kaolinite, and 0.37 m s^{-1} for bentonite; Table 2), C_m is the suspended-sediment concentration at $U_{h,m}$ (47% for silica flour, 22% for kaolinite, and 16% for bentonite), and C_0 is the threshold concentration above which the flow is not mobile enough to leave the reservoir ($U_h = 0$). The C_0 values were derived by extrapolation of the

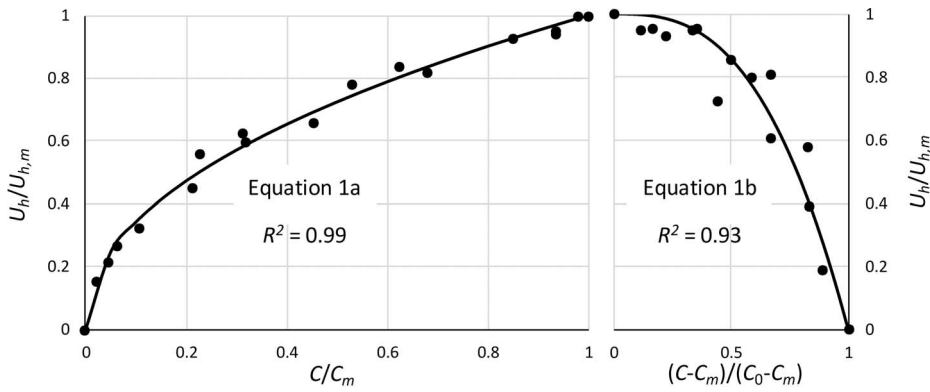


FIG. 11.—Nondimensional relationship between C and U_h for the kaolinite, bentonite, and silica-flour flows. Dots represent experimental data. Solid lines denote best-fit curves (Equations 1a, b).

experimental data to $U_h = 0$, yielding 20.5% for bentonite, 30.5% for kaolinite, and 53% for silica flour.

The best-fit Equations 1a and 1b have high R^2 values (probability value, $p \ll 0.05$; Fig. 11), confirming that the head-velocity curves for the bentonite, kaolinite, and silica-flour flows have a similar profile. Equation 1a describes the effect of density difference on head velocity in flows where turbulence is dominant and cohesive and frictional forces have a small influence on flow dynamics, or no influence at all. The power in Equation 1a is similar to the power of 0.5 in the well-known relationship between density difference and head velocity for experimental density currents by Keulegan (1957, 1958) and Middleton (1966):

$$U_h = 0.75 \left[\frac{(\rho_f - \rho_a)gH}{\rho_a} \right]^{0.5}, \quad (2)$$

where ρ_f is the flow density, ρ_a is the density of the ambient water, g is the acceleration due to gravity, and H is the flow thickness. Here, $\rho_f = \rho_s C + \rho_a(1-C) = \rho_a[sC + (1-C)]$, where ρ_s is the sediment density and s is the specific density of the sediment, ρ_s/ρ_a . The square-bracketed term in Equation 2 is equal to $(g'H)^{1/2}$, where $g' = g_s C$ is the reduced gravity of the sediment, where $g_s = (1-s)g$. Since the densimetric Froude number is defined by $Fr' = U_h/(g'H)^{1/2}$, Equation 2 states that the head velocity is governed by a densimetric Froude number of 0.75. This dimensional expression controls the approximate size of $U_{h,m}$ in Equations 1a, b. Assuming that C remains constant during the run and the volume per unit width is conserved $H = A/(0.31+x_h)$, where $A = 0.1085 \text{ m}^2$ is the cross-sectional area of the reservoir, and 0.31 m refers to the length of the reservoir, respectively, $U_{h,m} = 0.79 \text{ m s}^{-1}$ for silica flour, 0.41 m s^{-1} for kaolinite, and 0.24 m s^{-1} for bentonite.

Equation 1b describes the flows where the cohesive and frictional forces outbalanced the density difference and reduced the head velocity. The effect of these forces on head velocity is exponential, probably because the clay gelling and frictional interaction also caused rapid loss of turbulent particle support. Below, the exponents in Equations 1a and 1b are rounded to 0.5 and 3, respectively. These approximations do not cause a significant reduction in the R^2 values.

In the next step of the analysis, the dimensionless maximum head velocity, $U_h/U_{h,m}$, was related to the initial yield stress, τ_y , by using the dependence of yield stress on suspended-clay concentration, summarized in Table 2. These rheometrical data are available for kaolinite and bentonite clay only at concentrations greater than 1% (Table 2). The yield stresses for the bentonite and kaolinite suspensions that produced the flows with U_h values driven by the density difference with the ambient water ($C \leq C_m$) collapse well if plotted against C/C_m (Fig. 12A). This relationship can be described by a power law:

$$\tau_y = \tau_{y,m} (C/C_m)^3, \quad \text{for } 0 < C \leq C_m, \quad (3a)$$

with $R^2 = 0.94$ ($p \ll 0.05$) and $\tau_{y,m} = 37.9 \text{ N m}^{-2}$. $\tau_{y,m}$ is the yield stress

at $U_h = U_{h,m}$ and $C = C_m$. Hence, 37.9 N m^{-2} is the estimated initial yield stress at which U_h changed from being dominated by the density difference with the ambient water to being dominated by cohesive forces, independently of clay type. The yield stresses of the bentonite and kaolinite suspensions that produced the flows with U_h dominated by cohesion ($C > C_m$) collapse if plotted against $(C-C_m)/(C_0-C_m)$ (Fig. 12B):

$$\tau_y = \tau_{y,m} + (\tau_{y,0} - \tau_{y,m}) \left(\frac{C - C_m}{C_0 - C_m} \right)^3, \quad \text{for } C_m < C \leq C_0, \quad (3b)$$

With $R^2 = 0.96$ ($p \ll 0.05$) and $\tau_{y,0} = 271 \text{ N m}^{-2}$. $\tau_{y,0}$ is the estimated yield stress at $C = C_0$ and $U_h = 0$, thus representing the yield stress above which the clay suspensions did not leave the reservoir, regardless of clay type.

Equations 1a, 1b, 3a, and 3b can now be combined to derive relationships between τ_y and $U_h/U_{h,m}$ with $R^2 = 0.82$ ($p \ll 0.05$; Fig. 13):

$$\frac{U_h}{U_{h,m}} = \left(\frac{\tau_y}{\tau_{y,m}} \right)^{1/6}, \quad \text{for } 0 < \tau_y \leq \tau_{y,m}, \quad (4a)$$

$$\frac{U_h}{U_{h,m}} = \frac{\tau_{y,0} - \tau_y}{\tau_{y,0} - \tau_{y,m}}, \quad \text{for } \tau_{y,m} < \tau_y \leq \tau_{y,0} \quad (4b)$$

In experiments where the runout distance was beyond the end of the tank, Hallworth et al.'s (1998) box model was used to estimate the expected runout distance. This model, which is for noncohesive flows, assumes that the Froude number at the head of the flow is constant, the volume is conserved, and the settling is unhindered. The runout distance, x_0 , corresponding to the time for all the sediment to settle out, is

$$x_0 = QC^{1/5}, \quad (5)$$

where Q is a constant for each sediment type, which is dependent on the sediment density, grain diameter, settling velocity, and the cross-sectional area of the reservoir. Hallworth and Huppert (1998) demonstrated that Hallworth et al.'s (1998) model predicts the runout distance well, provided that $C < 15\%$. Based on fitting to the velocities for the 1% and 5% runs for each sediment (Figs. 3A, 6A, 7A), Appendix A demonstrates that x_0 can be estimated and shows that $Q = 21 \text{ m}$ for silica flour and $Q = 20 \text{ m}$ for kaolinite and bentonite. For concentrations in the range $1\% \leq C \leq 15\%$ and using these Q values, Equation 5 correctly predicts runout distances that are greater than 4.69 m (cf. Fig. 14A).

The dependence of runout distance on concentration for the high-concentration flows in Figure 10B is approximately linear. Therefore, anticipating that there is a crossover between this straight-line fit and the runout distance of the low-concentration flows, predicted by Equation 5, a composite best-fit equation for $x_0/x_{0,m}$ can be defined as

$$\frac{x_0}{x_{0,m}} = \left(\frac{C}{C_{m1}} \right)^{1/5}, \quad \text{for } 0 < C \leq C_{m1}, \quad (6a)$$

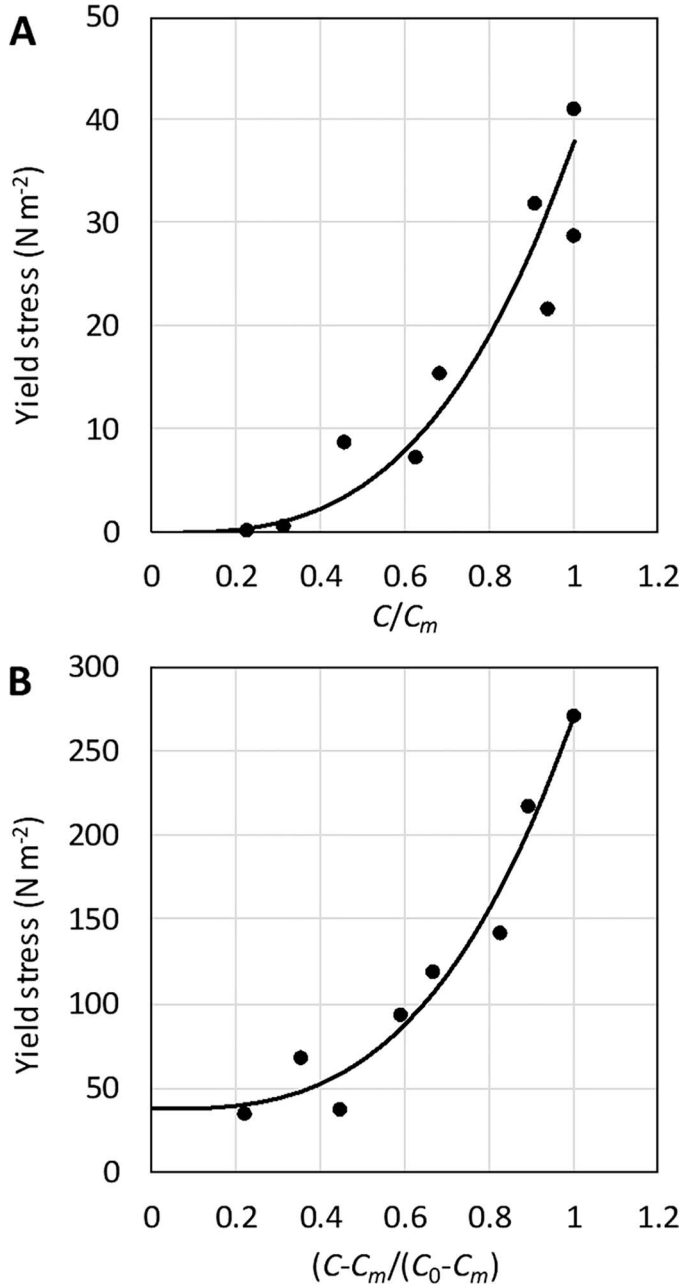


FIG. 12.—**A**) C/C_m against yield stress for bentonite and kaolinite at $C \leq C_m$. **B**) $(C-C_m)/(C_0-C_m)$ against yield stress for bentonite and kaolinite at $C > C_m$. Dots represent experimental data. Solid lines denote best-fit curves (Equations 3a, b).

$$\frac{x_0}{x_{0,m}} = \frac{C_0 - C}{C_0 - C_{m1}}, \quad \text{for } C_{m1} < C \leq C_0, \quad (6b)$$

where C_{m1} is the concentration at which the maximum runout distance, $x_{0,m}$, is reached. Using Equation 5, $x_{0,m} = Q C_{m1}^{1/5}$, C_{m1} was calculated as 29.8% for silica flour, 5.9% for kaolinite and 6.5% for bentonite. These values of C_{m1} are consistent with the assumption in Appendix A that $C = 1\%$ and 5% behave noncohesively and show $C_{m1} < C_m$. The maximum runout distance for silica flour is largest, $x_{0,m} = 16.5$ m, and the maximum runout distances for kaolinite and bentonite are smaller and similar, $x_{0,m} = 11.4$ m and 11.3 m (Fig. 14A). The linear fit to the data based on Equation 6b yielded $R^2 = 0.97$ ($p \ll 0.05$; Fig. 14B).

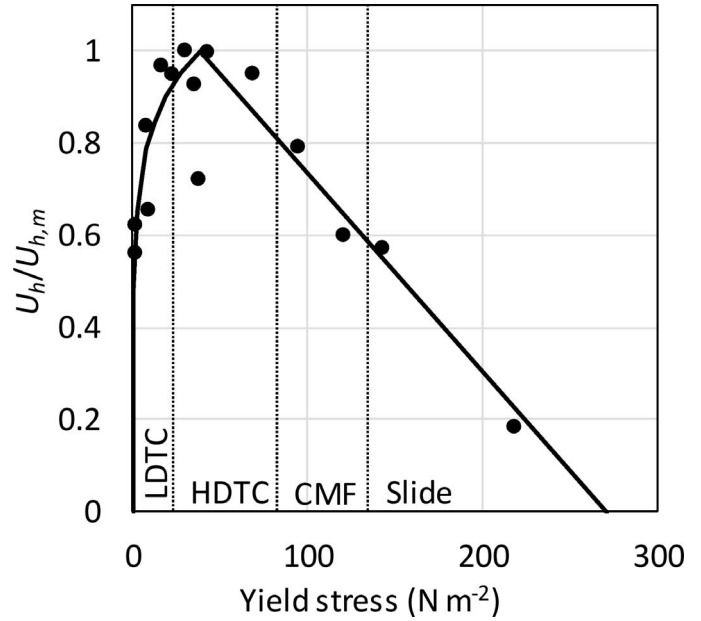


FIG. 13.— $U_h/U_{h,m}$ against yield stress for kaolinite and bentonite. Dots represent experimental data. Solid line denotes best-fit curve (Equations 4a, b). LDTC, low-density turbidity current; HDTC, high-density turbidity current; CMF, cohesive mud flow. Boundaries between flow types are average yield-stress values based on the ranges in Table 3.

Equations 3 and 6 can now be combined to derive relationships between τ_y and $x_0/x_{0,m}$:

$$\frac{x_0}{x_{0,m}} = \begin{cases} \left(\frac{\tau_y}{\tau_{y,m1}}\right)^{1/15}, & \text{for } 0 < \tau_y \leq \tau_{y,m1}, \\ \frac{C_0 - C_m(\tau_y/\tau_{y,m})^{1/3}}{C_0 - C_{m1}}, & \text{for } \tau_{y,m1} < \tau_y \leq \tau_{y,m}, \\ \left(\frac{C_0 - C_m}{C_0 - C_{m1}}\right) \left[1 - \left(\frac{\tau_y - \tau_{y,m}}{\tau_{y,0} - \tau_{y,m}}\right)^{1/3}\right], & \text{for } \tau_{y,m} < \tau_y \leq \tau_{y,0}, \end{cases} \quad (7)$$

where $\tau_{y,m1} = \tau_{y,m}(C_{m1}/C_m)^3$, with $\tau_{y,m1} = 0.74$ N m⁻² for kaolinite and $\tau_{y,m1} = 2.52$ N m⁻² for bentonite. Equation 7 for kaolinite and bentonite is compared with the data in Figure 15 ($R^2 = 0.71$; $p \ll 0.05$). It can be seen that there are only slight differences between the curves for the two sediments. Since $\tau_{y,m1}$ for kaolinite and bentonite are small compared to $\tau_{y,m}$, Equation 7 for $0 \leq \tau_y \leq \tau_{y,m}$, can be approximated by

$$\frac{x_0}{x_{0,m}} = 1 - \left(\frac{C_m - C_{m1}}{C_0 - C_{m1}}\right) \left(\frac{\tau_y}{\tau_{y,m}}\right)^{1/2}, \quad (8)$$

where the 1/2 power is based on matching the slope of x_0 at $\tau_y = \tau_{y,m}$ in Equation 7. Use of this approximation must be with the understanding that x_0 ultimately tends to zero as τ_y tends to zero. For kaolinite and bentonite, $(C_m - C_{m1})/(C_0 - C_{m1}) = 0.654$ and 0.679 and $(C_0 - C_m)/(C_0 - C_{m1}) = 0.346$ and 0.321 , such that $x_0/x_{0,m}$ can be approximated from Equations 7 and 8 by

$$\frac{x_0}{x_{0,m}} = 1 - \frac{2}{3} \left(\frac{\tau_y}{\tau_{y,m}}\right)^{1/2}, \quad \text{for } 0 \leq \tau_y \leq \tau_{y,m}, \quad (9a)$$

$$\frac{x_0}{x_{0,m}} = \frac{1}{3} \left[1 - \left(\frac{\tau_y - \tau_{y,m}}{\tau_{y,0} - \tau_{y,m}}\right)^{1/3}\right], \quad \text{for } \tau_{y,m} \leq \tau_y \leq \tau_{y,0}, \quad (9b)$$

which is also shown in Figure 15 ($R^2 = 0.68$; $p \ll 0.05$). In Equation 9, only $x_{0,m}$ is dependent on the box model (since $x_{0,m} = 11.4$ m and 11.3 m for kaolinite and bentonite, an average of these $x_{0,m}$ values could

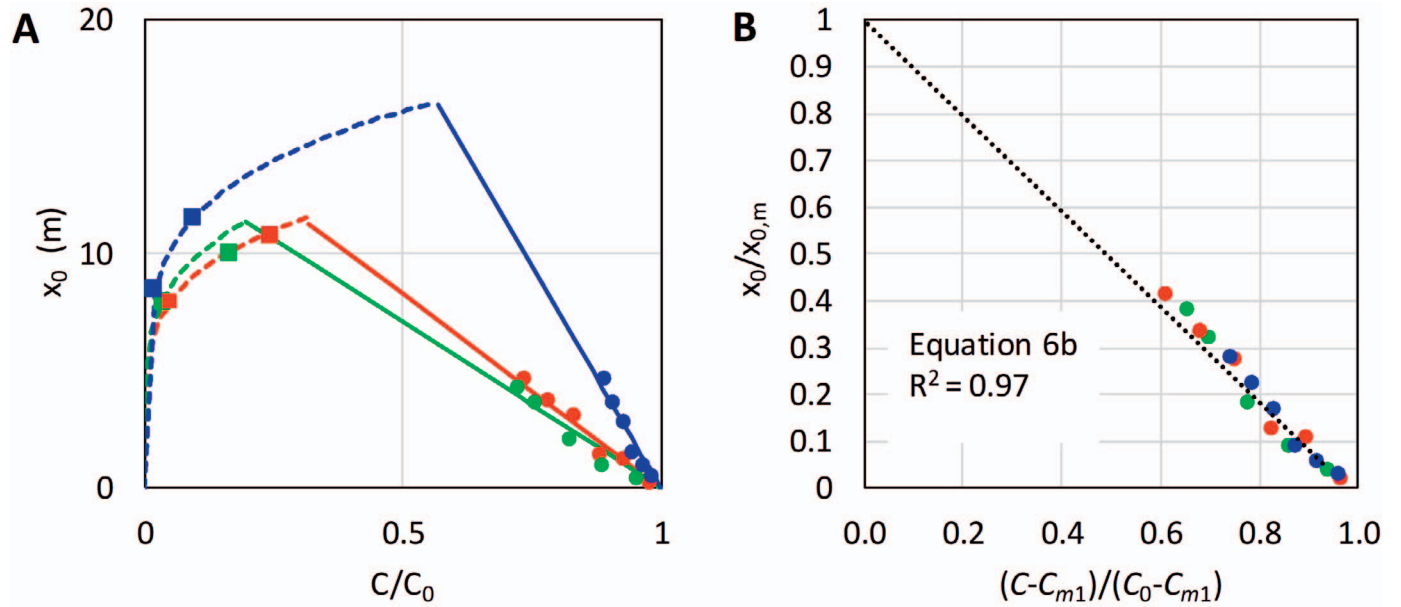


FIG. 14.—**A**) Runout distance, x_0 , against dimensionless concentration, C/C_0 for all flows. Circles denote the measured values given in Table 1. Squares are the extrapolated values given in Table A1. Solid lines represent fit to the data (Equation 6b), and dashed lines represent predictions by Hallworth and Huppert (1998) for low-concentration flows (Equation 5). The cross-over between these lines denotes the predicted maximum runout distance, $x_{0,m}$. **B**) Fit of $x_0/x_{0,m}$ to $(C-C_{m1})/(C_0-C_{m1})$ for all the experimental data, where $C > C_{m1}$. Colors as in Figure 10.

reasonably be taken). Equation 9 thus supports the hypothesis that the yield stress of the clay suspensions in the reservoir governs the variation in the runout distance of the clay flows after lifting the lock gate.

YIELD STRESS AS AN INDEPENDENT PARAMETER TO DESCRIBE FLOWS AND DEPOSITS

The above dimensional analysis demonstrates that fine-grained SGFs go through similar stages of flow dynamics and deposit properties with increasing initial suspended-sediment concentration. The differences in the cohesive properties of the clay suspensions were accounted for by converting suspended-sediment concentration to yield stress. This indicates that yield stress is a primary control on the head velocity and the runout distance. Equation 4 allows $U_h/U_{h,m}$ of a cohesive SGF to be estimated from the initial yield stress in a straightforward manner, independent of clay type. In addition, Equation 9 provides a simple tool for computing the runout distance of a cohesive SGF from its initial yield stress, also independent of clay type. At present, however, the determination of the maximum head velocity requires knowledge of $U_{h,m}$, which is dependent on clay type. The dimensional analysis is based on the initial τ_y value of the suspensions in the reservoir. Once these suspensions flow out of the reservoir, the yield stress of the SGFs can be expected to vary in space and time as a result of mixing with ambient water and sediment deposition, as clay bonds break and reform under the changing flow stresses. However, the results of the dimensional analysis imply that these variations have little effect on the nondimensional maximum head velocity and the runout distance of these experimental flows, if the yield stress of the bentonite and kaolinite clay in the reservoir is identical.

Table 3 summarizes the properties of the LDTCs, HDTCs, mud flows, and slides, and their deposits. Despite the large differences in initial suspended-sediment concentration of the three types of sediment, these flow types have similar shapes, internal dynamics, and deposit shapes. The HDTCs produced deposits that were wedge-shaped with a block-shaped extensions, the CMFs and NCMF produced wedge-shaped deposits with outrunner blocks, and the slides produced wedge-shaped deposits without

extension (Table 3). These deposit shapes were clearly linked to the flow behavior of the fine-grained SGFs and the balance between the processes that promote and impede flow. The properties of the four flow types and their deposits are bracketed by yield stress in Table 3. LDTCs change to HDTCs at $\tau_y \approx 16\text{--}22 \text{ N m}^{-2}$, the boundary between HDTCs and CMFs is at $\tau_y \approx 67\text{--}94 \text{ N m}^{-2}$, and slides are stable between $\tau_y \approx 119\text{--}141 \text{ N m}^{-2}$ and $\tau_y \approx 271 \text{ N m}^{-2}$.

WIDER IMPLICATIONS

The present laboratory experiments are a suitable starting point for determining the dynamic properties, runout distance, and deposit geometry of fine-grained SGFs in the natural environment, based on differences in rheology. However, quantitative scaling of the experimental results to natural flows and their deposits is not possible at present, principally because the best-fit coefficients in Equations 1 and 3–9 and the value of $\tau_{y,m}$ might be dependent on the experimental setup. For example, the experiments were limited to flows carrying a single sediment type and moving across a horizontal bed with a low bed roughness, and to a single set of potential energies, controlled by the height of the suspension column in the reservoir.

Notwithstanding these limitations, the experimental data can be used to make a qualitative comparison with full-scale flows in nature. The laboratory flows with $C \leq 10\%$ behaved in a similar manner for the three sediment types, with turbulence dominating these flows and the sediment particles unable to form high enough frictional forces or electrostatic forces of attraction to limit flow mobility. It is expected that the shape of the deposits of these LDTCs is also independent of the cohesive properties of the sediment, although a longer lock-exchange tank is needed to test this hypothesis. Based on previous work (e.g., Middleton 1967; Lüthi 1981; Bonnecaze et al. 1993; Amy et al. 2005), these turbidite deposits should be elongate, thin, and wedge-shaped. The threshold concentration of 10% might be higher for natural flows, since full-scale turbidity currents are often more turbulent (Talling et al. 2013), and therefore more likely to break the bonds between clay particles, than laboratory-scale turbidity

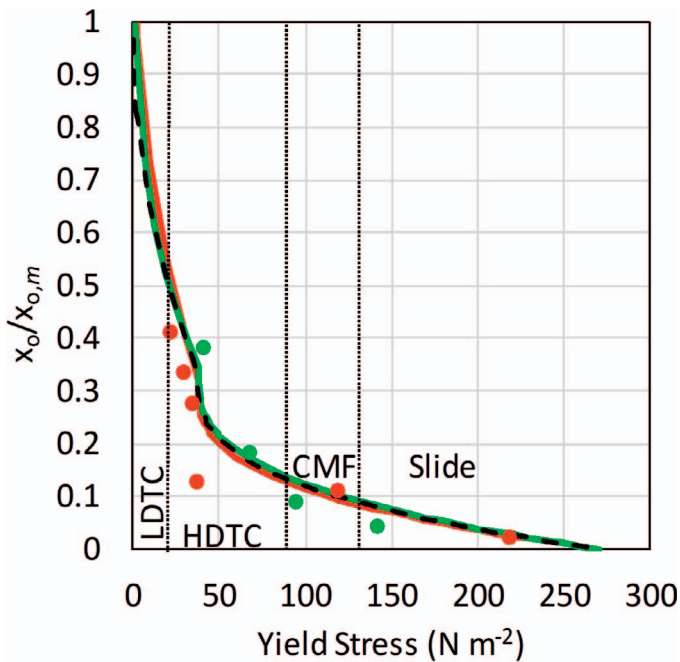


FIG. 15.—Dimensionless deposit runout distances of the clay flows against yield stress for kaolinite (green) and bentonite (red). Dots represent experimental data. Solid lines denote curves according to Equation 7 for kaolinite and bentonite (for clarity, yield stresses where $\tau_y < \tau_{y,m1}$ have not been plotted) and the dashed line denotes the curve according to Equation 9. LDTC, low-density turbidity current; HDTC, high-density turbidity current; CMF, cohesive mud flow. Boundaries between flow types are average yield stress values based on the ranges in Table 3.

currents. For practical purposes, this outcome implies that the deposits of clay-size and fine-silt size LDTCs can be interpreted in terms of turbulence properties and density difference with the ambient water, and that the type of sediment and yield stress can be ignored, even if these flows carry strongly cohesive clay minerals, such as bentonite. In other words, clay- and silt-laden LDTCs have similar flow efficiencies (*sensu* Mutti et al. 1999).

In contrast, the type of sediment and the yield stress need to be taken into account for most HDTCs, mud flows, and slides. These high-density SGFs should generally transport weakly cohesive kaolinite over a greater distance than strongly cohesive bentonite, whilst noncohesive fine-grained SGFs are inferred to travel the greatest distance from the origin. Hence, the flow efficiency of HDTCs, mud flows, and slides is generally lower for bentonite than for kaolinite (Mutti et al. 1999). The high efficiency of the laboratory flows laden with up to 47% silica flour is remarkable, and the anticipated implications for natural flows are significant. These laboratory flows were driven by a high-density difference with the ambient water, high turbulence intensity, and low particle settling velocity. Natural turbidity currents may be at least one order of magnitude faster than in the laboratory (Talling et al. 2013). Since turbulence intensity increases with increasing flow velocity (e.g., Baas et al. 2009), natural turbidity currents should be able to carry large volumes of silt-size particles over long distances. This high sediment flux and long transport distance may even extend to sand-size particles (cf. Talling et al. 2007), if turbulent forces are sufficiently strong to keep the sand particles in suspension and frictional forces between the sand particles are weak. It is clear that the runout distance of SGFs also depends on other factors, such as flow volume, basin-floor morphology, and the ratio of cohesive to noncohesive sediment (Talling 2013). However, it is concluded here that fine-sediment type is a major control above suspended-sediment concentrations that are equivalent to the laboratory threshold of 10%, and that flow efficiency reaches a

maximum value at which frictional and cohesive forces become dominant over density difference and particle support by turbulence. Once past this maximum, the flow efficiency rapidly decreases.

The rheological control on flow properties may also have significant implications for the geometry of the deposits of high-density SGFs. It is expected that, at similar C values, the deposits of high-density SGFs laden with weakly cohesive clay cover a larger surface area and have a smaller bed thickness than the deposits of high-density SGFs laden with strongly cohesive clay. Conversely, weakly cohesive clay beds may be thicker than their strongly cohesive equivalents, if these beds were formed by flows with the same initial yield strength, because flows laden with strongly cohesive clay carry a smaller volume of sediment, and were predicted to have approximately the same runout distance as the flows laden with weakly cohesive clay (Fig. 15; Equation 9).

Kaolinite and bentonite are the weakly and strongly cohesive end members of a suite of clay minerals that are common in nature (Table 1). Illite and chlorite are clay minerals of intermediate cohesive strength. Further work is needed to verify if the rheological model for kaolinite and bentonite SGFs presented in this study is also valid for chlorite and illite SGFs, and also stretches to SGFs that carry mixtures of clay minerals. This study covered the entire spectrum from noncohesive to strongly cohesive sediment, so it is appropriate to hypothesize that measuring the relationship between yield stress and suspended-sediment concentration for, for example, illite, chlorite, and mixed clay minerals is sufficient to determine the flow dynamics, runout distance, and deposit shape of SGFs laden with these types of sediments, notwithstanding the limitations described above. This hypothesis assumes that other clay minerals do not have more complex rheological properties than kaolinite and bentonite.

With time, recurring SGF events build the architecture of larger-scale sediment bodies, such as channel fills, levees, and lobes in submarine fans. It follows from the above discussion that this architecture may be different for flows that carry different types of clay minerals and noncohesive fine sediment, especially if HDTCs, mud flows, and slides constitute a major portion of this architecture. Other potential geological applications of this study include: (i) a better delineation of the rheological properties of SGFs that form LDTC deposits, HDTC deposits, debris flows, and slides in core and outcrop, and (ii) rheological characterization of modern turbidity currents in lakes and oceans, based on novel techniques for measuring flow velocity and suspended-sediment concentration (e.g., Sumner and Paull 2014).

CONCLUSIONS

The present laboratory experiments show that both sediment type and suspended-sediment concentration control the flow properties and the deposits of fine-grained SGFs. At low concentrations, the dominant turbulent forces prevent electrochemical binding and frictional interaction between the particles, and the density difference with the ambient water drives the flow, thus producing similar behavior between flows laden with sediment of contrasting cohesive properties. At high concentrations, however, cohesive and frictional forces outbalance turbulent forces, leading to decreased particle support in the flow. Consequently, noncohesive silica-flour flows produce a greater runout distance and a higher maximum head velocity, U_h , than weakly cohesive kaolinite flows of similar density. This difference in flow behavior is even greater for strongly cohesive bentonite flows, which have the shortest runout distances and the lowest U_h . The change in flow behavior controlled by density difference and turbulent forces to flow behavior controlled by cohesive or frictional forces increased from 16% for bentonite via 22% for kaolinite to 47% for silica flour. This threshold concentration for the silica-flour flows is close to the cubic packing density of clastic sediment, which supports the idea that noncohesive fine-grained SGFs are turbulent and highly mobile up to

very high densities, and friction between particles in an extremely dense suspension is required to impede flow.

The SGFs laden with silica flour, kaolinite, and bentonite changed from LDTCs via HDTCs and mud flows to slides as C was increased. Within the limits of the experimental setup, these flow types have similar flow properties and produce similar deposit shapes. The initial yield stress of the pre-failure suspension defines the transition between these flow types, and τ_y also governs the dimensionless maximum head velocity and the runout distance of these SGFs, independently of clay type. In other words, the present study demonstrates that yield stress is a primary control on the momentum and the runout distance of fine-grained SGFs.

This laboratory study provides an exciting platform for increasing the understanding and the predictive ability of the shape and the runout length of the deposits of natural fine-grained SGFs. The effect of the cohesive properties of the suspended sediment on deposit geometry can be ignored only at $C \leq 10\%$. Above this concentration, the runout length of the deposits increases, as the cohesive properties of the suspended sediment decrease. However, it should be noted that this threshold concentration is probably higher for natural flows, because these are often more turbulent than the laboratory flows. The differences in the geometry of deposits from flows laden with fine-grained sediment of contrasting cohesive strength may be reflected in differences in the architecture of stacked fine-grained SGF deposits.

ACKNOWLEDGMENTS

We are very grateful to Statoil for funding MLB's PhD studentship and to the U.K. Natural Environment Research Council for grant NE/I027223/1 (COHBED) that enabled this research to be undertaken, using the flume facility kindly built by Bangor University technician Rob Evans. We also thank Brian Scannell, Sophie Wilmes, Ben Barton, and Nathan Howard for their help in the laboratory. Katrien Van Landeghem and Connor McCarron gave us access to the SeaTek ranging system and kindly assisted in the set-up. Mauricio Perillo and Viktor Terlaky are thanked for their helpful reviews that greatly improved this manuscript. We are also grateful to JSR Editor Gary Hampson and Associate Editor Bill McCaffrey for their constructive comments and suggestions. Corresponding Editor John Southard is thanked for his attentive editing of the manuscript.

REFERENCES

- AMY, L.A., TALLING, P.J., PEAKALL, J., WYNN, R.B., AND ARZOLA THYNNE, R.G., 2005, Bed geometry used to test recognition criteria of turbidites and (sandy) debrites: *Sedimentary Geology*, v. 179, p. 163–174.
- ATKINSON, J., 2007, *The Mechanics of Soils and Foundations*: London, CRC Press, 442 p.
- BAAS, J.H., 2005, Sediment gravity flows: recent advances in process and field analysis: introduction: *Sedimentary Geology*, v. 179, p. 1–3.
- BAAS, J.H., AND BEST, J.L., 2002, Turbulence modulation in clay-rich sediment-laden flows and some implications for sediment deposition: *Journal of Sedimentary Research*, v. 72, p. 336–340.
- BAAS, J.H., VAN KESTEREN, W., AND POSTMA, G., 2004, Deposits of depletive high-density turbidity currents: a flume analogue of bed geometry, structure and texture: *Sedimentology*, v. 51, p. 1053–1088.
- BAAS, J.H., MCCAFFREY, W.D., HAUGHTON, P.D.W., AND CHOUX, C., 2005, Coupling between suspended sediment distribution and turbulence structure in a laboratory turbidity current: *Journal of Geophysical Research: Oceans*, v. 110, p. 1–20.
- BAAS, J.H., BEST, J.L., PEAKALL, J., AND WANG, M., 2009, A phase diagram for turbulent, transitional, and laminar clay suspension flows: *Journal of Sedimentary Research*, v. 79, p. 162–183.
- BAAS, J.H., BEST, J.L., AND PEAKALL, J., 2016, Comparing the transitional behavior of kaolinite and bentonite suspension flows: *Earth Surface Processes and Landforms*, v. 41, p. 1911–1921.
- BARKER, S.P., HAUGHTON, P.D.W., MCCAFFREY, W.D., ARCHER, S.G., AND HAKES, B., 2008, Development of rheological heterogeneity in clay-rich high-density turbidity currents: Aptian Britannia Sandstone Member, U.K. continental shelf: *Journal of Sedimentary Research*, v. 78, p. 45–68.
- BLACKBOURN, G.A., AND THOMSON, M.E., 2000, Britannia Field, UK North Sea: petrographic constraints on Lower Cretaceous provenance, facies, and the origin of slurry-flow deposits: *Petroleum Geoscience*, v. 6, p. 329–343.
- BONNECAZE, R.T., HUPPERT, H.E., AND LISTER, J.R., 1993, Particle-driven gravity currents: *Journal of Fluid Mechanics*, v. 250, p. 339–369.
- BRITTER, R.E., AND SIMPSON, J.E., 1978, Experiments on the dynamics of a gravity current head: *Journal of Fluid Mechanics*, v. 88, p. 223–240.
- CARTIGNY, M.J.B., EGGENHUISEN, J.T., HANSEN, E.W.M., AND POSTMA, G., 2013, Concentration-dependent flow stratification in experimental high-density turbidity currents and their relevance to turbidite facies models: *Journal of Sedimentary Research*, v. 83, p. 1046–1064.
- DE LEEUW, J., EGGENHUISEN, J.T., AND CARTIGNY, M.J.B., 2016, Morphodynamics of submarine channel inception revealed by new experimental approach: *Nature Communications*, v. 7, no. 10886.
- DROZ, L., MARSET, T., ONDRE, H., LOPEZ, M., AND SAVOYE, B., 2003, Architecture of an active mud-rich turbidite system: the Zaire Fan (Congo–Angola margin southeast Atlantic): results from ZaiAngo 1 and 2 cruises: *American Association of Petroleum Geologists, Bulletin*, v. 87, p. 1145–1168.
- DYER, K.R., AND MANNING, A.J., 1999, Observation of the size, settling velocity and effective density of flocs, and their fractal dimensions: *Journal of Sea Research*, v. 41, p. 87–95.
- ELVERHØI, A., ISSLER, D., DE BLASIO, F.V., ILSTAD, T., HARBITZ, C.B., AND GAUER, P., 2005, Emerging insights into the dynamics of submarine debris flows: *Natural Hazards and Earth System Science*, v. 5, p. 633–648.
- FELIX, M., AND PEAKALL, J., 2006, Transformation of debris flows into turbidity currents: mechanisms inferred from laboratory experiments: *Sedimentology*, v. 53, p. 107–123.
- GRIFFIN, J.J., WINDOM, H., AND GOLDBERG, E.D., 1968, The distribution of clay minerals in the world ocean: *Deep-Sea Research*, v. 15, p. 433–459.
- HALLWORTH, M.A., AND HUPPERT, H.E., 1998, Abrupt transitions in high-concentration, particle-driven gravity currents: *Physics of Fluids*, v. 10, p. 1083–1087.
- HALLWORTH, M.A., HOGG, A.J., AND HUPPERT, H.E., 1998, Effects of external flow on compositional and particle gravity currents: *Journal of Fluid Mechanics*, v. 359, p. 109–142.
- HAMPTON, M.A., 1972, The role of subaqueous debris flow in generating turbidity currents: *Journal of Sedimentary Petrology*, v. 42, p. 775–793.
- HAMPTON, M.A., 1975, Competence of fine-grained debris flows: *Journal of Sedimentary Petrology*, v. 45, p. 833–844.
- HEALY, T., WANG, Y., AND HEALY, J.A., 2002, *Muddy Coasts of the World: Processes, Deposits and Function*: Amsterdam, Elsevier, 556 p.
- HEEZEN, B.C., MENZIES, R.J., SCHNEIDER, E.D., EWING, W.M., AND GRANELLI, N.C.L., 1964, Congo Submarine Canyon: *American Association of Petroleum Geologists, Bulletin*, v. 48, p. 1126–1149.
- HILLEL, D., 2004, *Introduction to Environmental Soil Physics*: Amsterdam, Elsevier Academic Press, 494 p.
- HILLIER, S., 1995, Erosion, sedimentation and sedimentary origin of clays, *in* Velde, B., ed., *Origin and Mineralogy of Clays*: Berlin, Springer, p. 162–219.
- HOLTZ, R.D., AND KOVACS, W.D., 1981, *An Introduction of Geotechnical Engineering*: New York, Prentice Hall, 733 p.
- HUPPERT, H.E., AND SIMPSON, J.E., 1980, The slumping of gravity currents: *Journal of Fluid Mechanics*, v. 99, p. 785–799.
- IVERSON, R.M., 1997, The physics of debris flows: *Reviews of Geophysics*, v. 35, p. 245–296.
- JACOBSON, M.R., AND TESTIK, F.Y., 2013, On the concentration structure of high-concentration constant-volume fluid mud gravity currents: *Physics of Fluids*, v. 25, no. 016602.
- KANE, I.A., AND PONTÉN, A.S.M., 2012, Submarine transitional flow deposits in the Paleogene Gulf of Mexico: *Geology*, v. 40, p. 1119–1122.
- KANE, I.A., DYKSTRA, M.L., KNELLER, B.C., TREMBLAY, S., AND MCCAFFREY, W.D., 2009, Architecture of a coarse-grained channel–levee system: the Rosario Formation, Baja California, Mexico: *Sedimentology*, v. 56, p. 2207–2234.
- KANE, I.A., MCCAFFREY, W.D., PEAKALL, J., AND KNELLER, B.C., 2010, Submarine channel levee shape and sediment waves from physical experiments: *Sedimentary Geology*, v. 223, p. 75–85.
- KEEVIL, G.M., PEAKALL, J., BEST, J.L., AND AMOS, K.J., 2006, Flow structure in sinuous submarine channels: velocity and turbulence structure of an experimental submarine channel: *Marine Geology*, v. 229, p. 241–257.
- KEULEGAN, G.H., 1957, Thirteenth progress report on model laws for density currents: an experimental study of the motion of saline water from locks into fresh water channels: U.S. Department of Commerce, National Bureau of Standards, v. 5168.
- KEULEGAN, G.H., 1958, Twelfth progress report on model laws for density currents: the motion of saline fronts in still water U.S. Dept. of Commerce, National Bureau of Standards, v. 5831.
- KHABBAZI BASMENJ, A., MIRJAVAN, A., GHAFORI, M., AND CHESHOMI, A., 2017, Assessment of the adhesion potential of kaolinite and montmorillonite using a pull-out test device: *Bulletin of Engineering Geology and the Environment*, p. 1–13.
- KNELLER, B., AND BUCKEE, C., 2000, The structure and fluid mechanics of turbidity currents: a review of some recent studies and their geological implications: *Sedimentology*, v. 47, p. 62–94.
- KOISTRA, A., VERHOEF, P.N.W., BROERE, W., NGAN-TILLARD, D.J.M., AND VANTOL, A.F., 1998, Appraisal of stickiness of natural clays from laboratory tests, *in* 25th National Symposium of Engineering Geology, Proceedings, Delft, Netherlands, p. 101–113.

- KUENEN, P.H., 1951, Properties of turbidity currents of high density: Society of Economic Palaeontologists and Mineralogists, Special Publication v. 2, p. 14–33.
- KUENEN, P.H., AND MIGLIORINI, C.I., 1950, Turbidity currents as a cause of graded bedding: *The Journal of Geology*, v. 58, p. 91–127.
- LAGALY, G., 1989, Principles of flow of kaolin and bentonite dispersions: *Applied Clay Science*, v. 4, p. 105–123.
- LOWE, D.R., 1982, Sediment gravity flows: II. Depositional models with special reference to high density turbidity currents: *Journal of Sedimentary Petrology*, v. 52, p. 279–297.
- LOWE, D.R., AND GUY, M., 2000, Slurry-flow deposits in the Britannia Formation (Lower Cretaceous), North Sea: a new perspective on the turbidity and debris flow problem: *Sedimentology*, v. 47, p. 31–70.
- LUCKHAM, P., AND ROSSI, S., 1999, The colloidal and rheological properties of bentonite suspensions: *Advances in Colloid and Interface Science*, v. 82, p. 43–92.
- LUTHI, S., 1981, Experiments on non-channelized turbidity currents and their deposits: *Marine Geology*, v. 40, p. 59–68.
- MARR, J.G., SHANMUGAM, G., AND PARKER, G., 2001, Experiments on subaqueous sandy gravity flows: the role of clay and water content in flow dynamics and depositional structures: *Geological Society of America, Bulletin*, v. 113, p. 1377–1386.
- MARTINSEN, O., 1994, Mass Movements, *in* Maltman, A., ed., *The Geological Deformation of Sediments*: London, Chapman and Hall, p. 127–165.
- MIDDLETON, G.V., 1966, Experiments on density and turbidity currents. I. Motion of the head: *Canadian Journal of Earth Sciences*, v. 3, p. 523–546.
- MIDDLETON, G.V., 1967, Experiments on density and turbidity currents. III. Deposition of sediment: *Canadian Journal of Earth Sciences*, v. 4, p. 475–505.
- MIDDLETON, G., 1993, Sediment deposition from turbidity currents: *Annual Review of Earth and Planetary Sciences*, v. 21, p. 89–114.
- MIDDLETON, G.V., AND HAMPTON, M.A., 1973, Sediment gravity flows: mechanics of flow and deposition, *in* Middleton, G.V., and Bouma, A.H., eds., *Turbidites and Deep Water Sedimentation*: SEPM, Pacific Coast Section, Short Course, Anaheim, California, p. 1–38.
- MIDDLETON, G.V., AND NEAL, W.J., 1989, Experiments on the thickness of beds deposited by turbidity currents: *Journal of Sedimentary Petrology*, v. 59, p. 297–307.
- MOHRIG, D., AND MARR, J.G., 2003, Constraining the efficiency of turbidity current generation from submarine debris flows and slides using laboratory experiments: *Marine and Petroleum Geology*, v. 20, p. 883–899.
- MOHRIG, D., WHIPPLE, K.X., HONDZO, M., ELLIS, C., AND PARKER, G., 1998, Hydroplaning of subaqueous debris flows: *Geological Society of America, Bulletin*, v. 110, p. 387–394.
- MULDER, T., AND ALEXANDER, J., 2001, The physical character of subaqueous sedimentary density flows and their deposits: *Sedimentology*, v. 48, p. 269–299.
- MUTTI, E., TINTERRI, R., REMACHA, E., MAVILLA, N., ANGELLA, S., AND FAVA, L., 1999, An introduction to the analysis of ancient turbidite basins from an outcrop perspective: *American Association of Petroleum Geologists, Continuing Education Course Note Series*, v. 39, 96 p.
- PARKER, G., GARCIA, M., FUKUSHIMA, Y., AND YU, W., 1987, Experiments on turbidity currents over an erodible bed: *Journal of Hydraulic Research*, v. 25, p. 123–147.
- PASHLEY, R., AND KARAMAN, M., 2004, *Applied Colloid and Surface Chemistry*: London, Wiley, 200 p.
- SCHINDLER, R.J., PARSONS, D.R., YE, L., HOPE, J.A., BAAS, J.H., PEAKALL, J., MANNING, A.J., ASPDEN, R.J., MALARKEY, J., SIMMONS, S., PATERSON, D.M., LICHTMAN, I.D., DAVIES, A.G., THORNE, P.D., AND BASS, S.J., 2015, Sticky stuff: redefining bedform prediction in modern and ancient environments: *Geology*, v. 43, p. 399–402.
- SUMNER, E.J., AND PAULL, C.K., 2014, Swept away by a turbidity current in Mendocino submarine canyon, California: *Geophysical Research Letters*, v. 41, p. 7611–7618.
- SUMNER, E.J., TALLING, P.J., AND AMY, L.A., 2009, Deposits of flows transitional between turbidity current and debris flow: *Geology*, v. 37, p. 991–994.
- TALLING, P.J., 2013, Hybrid submarine flows comprising turbidity current and cohesive debris flow: deposits, theoretical and experimental analyses, and generalized models: *Geosphere*, v. 9, p. 460–488.
- TALLING, P.J., AMY, L.A., WYNN, R.B., PEAKALL, J., AND ROBINSON, M., 2004, Beds comprising debrite sandwiched within co-genetic turbidite: origin and widespread occurrence in distal depositional environments: *Sedimentology*, v. 51, p. 163–194.
- TALLING, P.J., WYNN, R.B., MASSON, D.G., FRENZ, M., CRONIN, B.T., SCHIEBEL, R., AKHMETZHANOV, A.M., DALLMEIER-TIESSEN, S., BENETTI, S., WEAVER, P.P.E., GEORGIOPOULOU, A., ZÜHLSORF, C., AND AMY, L.A., 2007, Onset of submarine debris flow deposition far from original giant landslide: *Nature*, v. 450, p. 541–544.
- TALLING, P.J., PAULL, C.K., AND PIPER, D.J.W., 2013, How are subaqueous sediment density flows triggered, what is their internal structure and how does it evolve? Direct observations from monitoring of active flows: *Earth-Science Reviews*, v. 125, p. 244–287.
- TALLING, P.J., ALLIN, J., ARMITAGE, D.A., ARNOTT, R.W.C., CARTIGNY, M.J.B., CLARE, M.A., FELLETTI, F., COVAULT, J.A., GIRARDI, S., HANSEN, E., HILL, P.R., HISCOTT, R.N., HOGG, A.J., CLARKE, J.H., JOBE, Z.R., MALGESINI, G., MOZZATO, A., NARUSE, H., PARKINSON, S., PEEL, F.J., PIPER, D.J.W., POPE, E., POSTMA, G., ROWLEY, P., SGUAZZINI, A., STEVENSON, C.J., SUMNER, E.J., SYLVESTER, Z., WATTS, C., AND XU, J., 2015, Key future directions for research on turbidity currents and their deposits: *Journal of Sedimentary Research*, v. 85, p. 153–169.
- TAN, X., HU, L., REED, A.H., FURUKAWA, Y., AND ZHANG, G., 2014, Flocculation and particle size analysis of expansive clay sediments affected by biological, chemical, and hydrodynamic factors: *Ocean Dynamics*, v. 64, p. 143–157.
- VAN VLIET, T., 2013, *Rheology and Fracture Mechanics of Foods*: London, CRC Press, 363 p.
- VAN WEERING, T.C.E., AND VAN IPEREN, J., 1984, Fine-grained sediments of the Zaire deep-sea fan, southern Atlantic Ocean, *in* Stow, D.A.V., and Piper, D.J.W., eds., *Fine-Grained Sediments: Deep-Water Processes and Facies*: Geological Society of London, Special Publication 15, p. 95–113.
- WANG, Z., AND PLATE, E.C., 1996, A preliminary study on the turbulence structure of flows of non-Newtonian fluid: *Journal of Hydraulic Research*, v. 34, p. 345–361.
- WILSON, D., DAVIES, J., WALTERS, R., AND ZALASIEWICZ, J., 1992, A fault-controlled depositional model for the Aberystwyth Grits turbidite system: *Geological Magazine*, v. 129, p. 595–607.
- WINDOM, H.L., 1976, Lithogeneous material in marine sediments, *in* Riley, J.P., and Chester, R., eds., *Chemical Oceanography, Volume 5*: New York, Academic Press, p. 103–135.
- WINTERWERR, J.C., AND VAN KESTEREN, W.G.M., 2004, *Introduction to the Physics of Cohesive Sediment in the Marine Environment*: Oxford, U.K., Elsevier, *Developments in Sedimentology* 56, 559 p.
- XU, J.P., 2011, Measuring currents in submarine canyons: technological and scientific progress in the past 30 years: *Geosphere*, v. 7, p. 868–876.
- XU, J.P., SEQUEIROS, O.E., AND NOBLE, M.A., 2014, Sediment concentrations, flow conditions, and downstream evolution of two turbidity currents, Monterey Canyon, USA: *Deep-Sea Research Part I, Oceanographic Research Papers*, v. 89, p. 11–34.
- YONG, R.N., NAKANO, M., AND PUSCH, R., 2012, *Environmental Soil Properties and Behaviour*: London, CRC Press, 455 p.

Received 3 March 2017; accepted 5 September 2017.

APPENDIX

Determining the Runout Distances Using the Hallworth et al. (1998) Model for the 1% and 5% Flows

According to Hallworth et al. (1998), by defining a characteristic timescale, T , given by $T = (x_0^3 / Fr^2 g_s' C)^{0.5}$, the head velocity, U , nondimensionalized to TU/x_0 , can be expressed as

$$\chi = \xi^{-0.5} - \xi^2, \quad (\text{A1})$$

where $\xi = x/x_0$. When ξ is close to 1, the functional form of Equation A1 can be approximated by a simpler linear function:

$$\chi = 2.5(1 - \xi), \quad (\text{A2})$$

provided that $\xi > 0.288$ ($x > 0.288x_0$). Thus, the dimensional velocity can be fitted to a functional form given by $U = B_1 x^{-0.5} - B_2 x^2$ or $U = B_1 - B_2 x$, if the linear approximation can be applied, and $x_0 = (B_1/B_2)^{0.4}$ or B_1/B_2 . The 1% and 5% cases for silica flour are shown in Figure A1A. Since Equations A1 and A2 result in the velocity decreasing with increasing distance, only the part of the curve given by $x > x_s$, where $x_s = 2.5$ m, is included in the fit. For $x < x_s$, the current can be considered to be slumping and the assumption of a constant Froude number is not valid (Huppert and Simpson 1980). Thus, the linear fit can be used only if $x_s > 0.288x_0$. This criterion is satisfied for the 1% flows, but not for the 5% flows, so the nonlinear functional form must be used. Of the 1% and 5% flows, the 1% flow is considered the more reliable, because it requires less extrapolation and is likely to have the least cohesive behavior. The fit to the preferred runout distance for $C = 1\%$ on the basis of a $C^{1/5}$ dependence results in $Q = 21$ m in Equation 5. Figure A1B shows this $C^{1/5}$ dependence. Using a similar approach for kaolinite and bentonite, Q was determined to be 20 m for both clay types. There is little evidence of dependence on sediment grain size, density, or settling velocity (all reservoir cross-sectional areas are the same), since all three values of Q are similar. The preferred extrapolated runout distances for all 1% and 5% flows, which are used in the rest of the paper, are listed in Table A1.

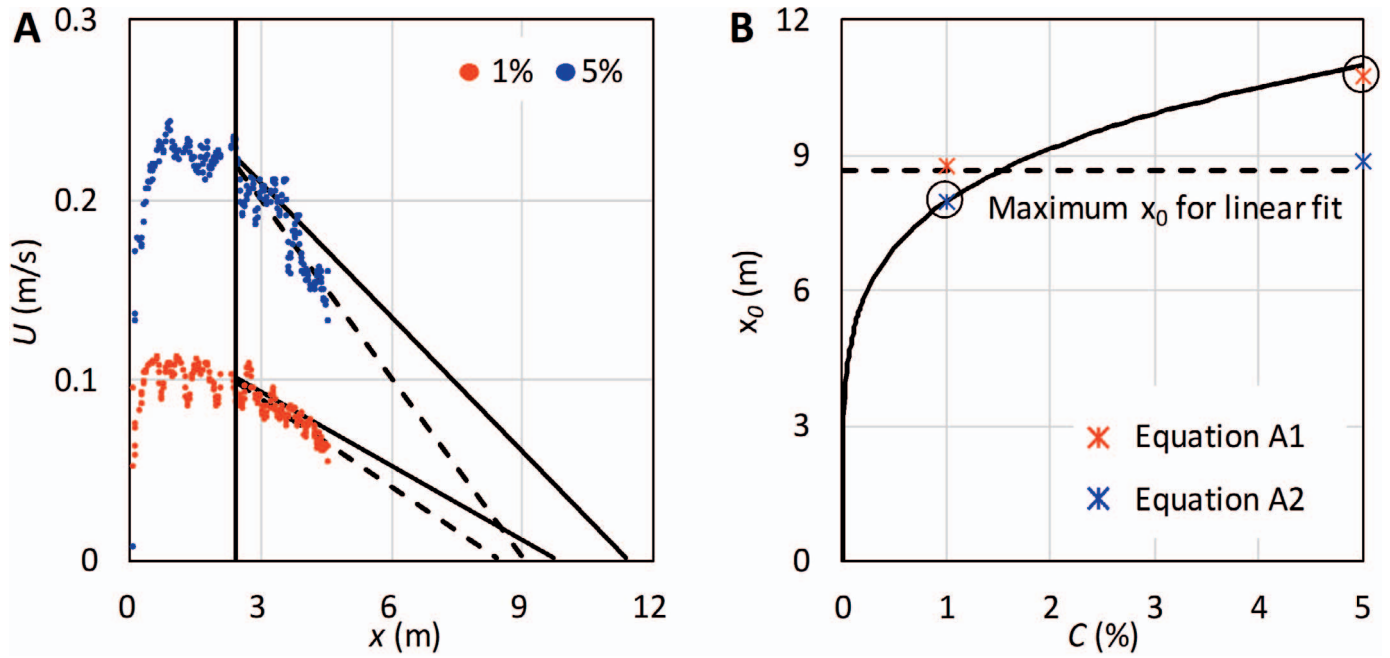


FIG. A1.—A) Determination of runout distance, x_0 , for the 1% and 5% silica-flour flows for $x > x_s$, using both Equation A1 (solid line) and Equation A2 (dashed line). B) Determination of the $C^{1/5}$ dependence for x_0 , based on the curve passing through the preferred x_0 at $C=1\%$. The preferred x_0 , with circle around symbol, is determined by the $x_0 \leq x_s/0.288$ condition for linear fitting.

TABLE A1.—Extrapolated runout distances (m).

Material	1%	5%
Silica flour	8.47	11.48
Kaolinite	7.87	10.00
Bentonite	8.00	10.76